

See discussions, stats, and author profiles for this publication at: <https://www.researchgate.net/publication/231374819>

# Novel Application of X-Ray Computed Tomography: Determination of Gas-Liquid Contact Area and Liquid Hold-Up in Structured Packing

ARTICLE *in* INDUSTRIAL & ENGINEERING CHEMISTRY RESEARCH · JULY 2007

Impact Factor: 2.59 · DOI: 10.1021/ie0701827

---

CITATIONS

26

---

READS

45

6 AUTHORS, INCLUDING:



[Richard Ketcham](#)

University of Texas at Austin

173 PUBLICATIONS 5,904 CITATIONS

SEE PROFILE

# Novel Application of X-ray Computed Tomography: Determination of Gas/Liquid Contact Area and Liquid Holdup in Structured Packing

Christian W. Green,<sup>†</sup> John Farone,<sup>†</sup> Julie K. Briley,<sup>†</sup> R. Bruce Eldridge,<sup>\*,†</sup>  
Richard A. Ketcham,<sup>‡</sup> and Ben Nightingale<sup>§</sup>

Separations Research Program, University of Texas, Austin, Texas 78712, Jackson School of Geosciences, University of Texas, Austin, Texas 78712, and General Electric Company, 1 Neumann Way–M/D Q8, Cincinnati, Ohio 45215

X-ray computed tomography (CT) was utilized to determine the effective wetted area and local liquid holdup for an air–water contactor containing structured packing. The experimental wetted area results were in agreement with results obtained from a traditional chemical absorption technique. The holdup varied significantly with vertical position. Areas near the joint region between adjacent packing elements exhibited holdup values greatly exceeding the values for holdup observed in the middle of the packing element. These findings will dramatically impact both design and model development for mass transfer devices containing structured packing

## 1. Introduction

### 1.1. Basic Principles of X-ray Computed Tomography.

X-ray computed tomography (CT) is used to noninvasively and nonintrusively obtain detailed cross-sectional images of objects, including the internal structure. Noninvasive imaging does not require sensors to be placed inside of the object for measurement and, therefore, does not alter the object being imaged. This makes X-ray CT a good choice for obtaining data otherwise unavailable from traditional methods of testing.

In X-ray CT, X-rays are transmitted through the object of interest and measured after they pass through the object. A material's linear attenuation coefficient,  $\mu$ , is a measure of the degree to which X-rays are attenuated when passing through a differential length of material,  $dL$ , as defined in eq 1.

$$\frac{dI}{I} = -\mu dL \quad (1)$$

For an object of uniform composition and length  $L$ , the final intensity of an X-ray beam with initial intensity  $I_0$  is given by eq 2. When the composition of the object is nonhomogeneous, the X-ray intensity is described by the more general eq 3, where nonconstant linear attenuation coefficients are integrated along the X-ray path,  $z$ .

Linear attenuation coefficients are proportional to the density of the material and generally increase with the atomic number of the material.<sup>1</sup> The coefficient is also dependent on the energy of the X-ray beam. Attenuation is typically more pronounced at lower X-ray intensities, which can be troublesome when a polyenergetic X-ray source is used.<sup>2</sup> As the beam passes through the object, X-rays of lower intensity will be preferentially attenuated, resulting in modification of the energetic profile of the X-ray beam. This phenomenon is known as beam hardening, and it results in an X-ray beam with higher average energy than the initial beam. Filters are often used to preharden the X-ray beam. However, beam hardening can still be significant in cases

where long lengths of extremely dense material are present along an X-ray path or when low-energy X-ray sources are used. In such cases, artifacts are often present in the reconstructed images. Image artifacts are features in an image that are not representative of the actual physical system being imaged. They may be caused by a variety of scenarios in addition to beam hardening.

$$I = I_0 e^{-\mu L} \quad (2)$$

$$I = I_0 e^{-\int \mu(z) dz} \quad (3)$$

The inverse Radon transform is the mathematical basis for X-ray CT. This relationship allows a function  $f(x,y)$  to be uniquely determined from an infinite set of line integrals of the same function. The desired function  $f(x,y)$  in the case of X-ray CT is the distribution of the object's linear attenuation coefficient, which can be mapped in two-dimensional coordinate space. The line integrals used to determine the function are the measured values of X-ray attenuation at different projections. By rearranging eq 3 to the form of eq 4, it is easier to see how the measured data relates to the line integrals. The attenuation data measured by the X-ray scanner is fed to an image reconstruction algorithm that approximates the inverse Radon transform. The output of the algorithm is an array that represents the linear attenuation coefficient at different points within the object space.

$$-\ln\left(\frac{I}{I_0}\right) = \int \mu(z) dz \quad (4)$$

**1.2. Equipment for X-ray Computed Tomography.** The configuration for an X-ray CT scanner requires an X-ray source and a set of detectors arranged on opposite sides of the object to be imaged. For most medical X-ray CT systems, the source and detectors are rotated around the object to obtain transmission data at a variety of radial positions. However, it is not uncommon for industrial X-ray CT scanners to rotate the object of interest and keep both the source and detectors fixed.

Transmission tomography in general involves a variety of different choices for radiation sources. Industrial systems

\* To whom all correspondence should be addressed. Tel.: (512) 232-1407. Fax: (512) 471-1720. E-mail: rbeldr@che.utexas.edu.

<sup>†</sup> Separations Research Program.

<sup>‡</sup> Jackson School of Geosciences.

<sup>§</sup> General Electric Company.

commonly employ isotope decay sources, X-ray tubes, or linear accelerators to produce X-rays for CT scanning purposes. Isotope sources usually produce X-ray beams of one energy level, although some isotope sources can produce two distinct energy levels. The X-ray flux of isotope sources is usually much lower than that of tube or linear accelerator sources. Linear accelerators are capable of producing higher energy X-rays than tube sources, although the beams produced by both types are polyenergetic. The higher energy X-rays produced by linear accelerators are necessary to avoid beam hardening when imaging large objects constructed of very dense materials, as is common for some industrial applications of X-ray CT.

The detectors used in X-ray CT applications generally fall into one of two categories. Scintillation detectors contain fluorescent material that visibly emits radiation when exposed to X-rays. Optical enhancement devices, such as photodiodes or photomultiplier tubes, are connected to the detector to convert the light emitted to an electrical signal. Ionization detectors typically use a Noble gas that produces a measurable current when energy is transferred to it by incident X-rays. Regardless of the detector style used, arrays can be constructed using a large number of detectors. These arrays are usually linear and can be either flat or curved, depending on the geometry of the X-ray beam. Some systems permit the effective area of the detectors to be varied by adjusting the aperture or considering only certain rows and columns from a digital detector. Adjusting the vertical aperture of the detectors is one way to control the thickness of a CT slice.

The X-ray transmission data necessary for image reconstruction may be obtained in a variety of ways. Several generations of CT scanner design have consistently improved the time required to obtain cross-sectional images. The first-generation scanner geometry consists of a point X-ray source and one detector. The source and detector are simultaneously translated to obtain measurements along a number of parallel ray paths. The source and detector are then rotated to a new angular position, and the translation process is repeated. The procedure continues until data has been acquired from  $180^\circ$ . A second-generation scanner utilizes a fan-beam X-ray source. This allows measurements to be obtained for several ray paths at once, although translation and rotation is still necessary to acquire a full set of transmission data.

Significant improvement is achieved with third- and fourth-generation scanning systems. For a third-generation system, a fan-beam source is used with multiple detectors arranged in a curved array. This eliminates the need for source and detector translation assuming the detectors are continuous, i.e., no space exists between adjacent detectors. Rotation is still required to acquire all data necessary for reconstruction. A fourth-generation scanning geometry contains a continuous set of detectors that comprise a circle around the object being scanned; only the fan-beam source is rotated.

The improvement of scanner design continues to be an active area of research. Recent developments include the use of multiple sources in a single scanner and the application of cone-beam sources combined with area detectors (two-dimensional detector arrays) to image a volume of the object rather than just a slice. Spiral scanning, where the simultaneous rotation and translation of the source and detectors or object occurs, allows for quick acquisition of a large set of volumetric data. Many of the applications first appear in the medical field and are subsequently adapted to industrial work. Advancements in scanner design usually necessitate improved or altogether new

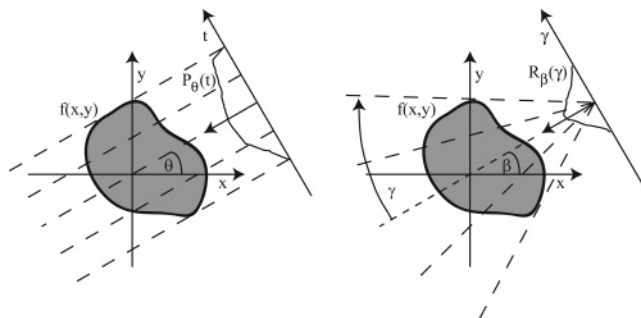


**Figure 1.** Geometry definitions for parallel-beam (left) and equiangular fan-beam (right) X-ray CT.

image reconstruction algorithms, particularly when the scanner geometry and method in which data are acquired have changed.

In addition to the source and detectors that are contained in a tomography system, the mechanical assembly is also of great importance. Precise control of the machinery used to manipulate the object, source, and detectors is critical. Image reconstruction algorithms as well as processing techniques applied to the resulting CT images depend on the manipulator moving with precision and being able to return to certain locations with exacting accuracy. The associated electronics must be designed to ensure proper communication between all related components of the system.

Depending on the geometry of the X-ray system, the transmission data that are collected represent a set of line integrals of the linear attenuation coefficient as was described by eq 4. The transmission data can be interpreted as either parallel-beam data or fan-beam data. Parallel-beam data are defined as functions of the angle  $\theta$  between the X-ray path lines and the axes of the object space, and the distance  $t$  of a given X-ray path from the center of rotation. For fan-beam geometry, the parameters describing the projection data include the angle between the central ray of the fan and the axes of the object space,  $\beta$ , and the angle  $\gamma$  between the central ray path and alternate ray paths. Figure 1 depicts the parameters for different scanner geometries in the object space and transmission data space. A sinogram is the result of displaying transmission data as an image, where the axes of the image are either  $\theta$  and  $t$  or  $\beta$  and  $\gamma$ , depending on the geometry used. When the location of a feature in the object is tracked through the image, a sine wave is produced, hence the name given to the image.

**1.3. Image Reconstruction for X-ray Computed Tomography.** Several standard image reconstruction algorithms have been presented by Leahy and Clackdoyle for both 2-D and 3-D data.<sup>3</sup> The two most commonly used algorithms are the algebraic reconstruction technique and the filtered backprojection method, which is implemented for the scanner used in this work.

The algebraic reconstruction technique, or ART, is one example of an iterative method for image reconstruction. The technique uses iteration to solve the system of line integral equations defined by the transmission data by altering an image matrix representing the object imaged. Convergence is achieved with the particular image matrix that provides the best fit to the data. This algorithm is particularly effective when the amount of available transmission data is low.

Filtered backprojection is clearly the most commonly used image reconstruction technique for X-ray CT applications. The mathematical basis for the technique is the Fourier slice theorem, which states that the one-dimensional Fourier transform of the parallel projection of an object at angle  $\theta$  corresponds to values along a radial line in the frequency domain, also at angle  $\theta$ , as shown in Figure 2.

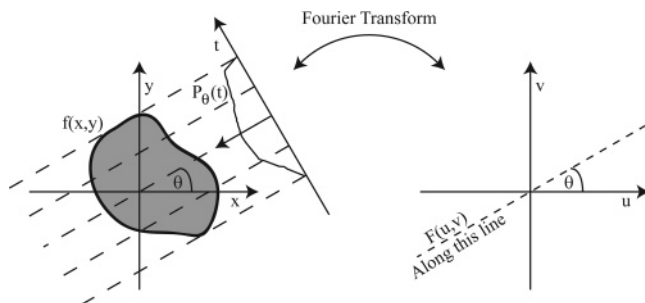


**Figure 2.** Illustration of Fourier slice theorem applied to parallel-beam X-ray CT transmission data (spatial domain on left, frequency domain on right).

For a function defined as  $f(x,y)$ , the Fourier transform  $F(u,v)$  is given by eq 5. Rosenfeld and Kak showed that the Fourier transform of an object's projection,  $S_\theta(w)$ , is equal to the Fourier transform of the function,  $F(u,v)$ .<sup>4</sup> Converting to polar coordinates in the frequency domain,  $u = w \cos \theta$  and  $v = w \sin \theta$ . Substituting these expressions results in eq 6.

$$F(u,v) = \int_{-\infty}^{\infty} \int_{-\infty}^{\infty} f(x,y) e^{-j2\pi(ux+vy)} dx dy \quad (5)$$

$$F(u,v) = F(w,\theta) = \int_{-\infty}^{\infty} P_\theta(t) e^{-j2\pi w t} dt = S_\theta(w) \quad (6)$$

Assuming the X-ray CT technique could acquire data for an infinite number of projections, the original function  $f(x,y)$  that represents the cross-sectional image could be reconstructed by applying the inverse Fourier transform. Regardless of how many projections are obtained using X-ray CT, they are still finite. This is one cause of image degradation. While this discussion has been focused on parallel-beam projection data, a similar result can be obtained for fan-beam data. Usually the fan-beam data is converted to parallel-beam data or a similar set of equations particular to fan-beam data are derived.

The filtered backprojection algorithm makes use of the Fourier slice theorem to reconstruct images from projection data. The first step is to take the Fourier transform of the projection data as shown in eq 6. Filters are applied to the projection data in the frequency domain to improve the quality of the image by reducing noise and improving sharpness. Shown in eq 7, the filtered projection,  $Q_\theta(t)$ , is determined by approximating  $|w|$  via a mathematical filter and applying the inverse Fourier transform. Examples of filters commonly used in filtered backprojection algorithms are the Ram-Lak, low-pass cosine, Hamming, and Shepp-Logan filters.<sup>5</sup>

$$Q_\theta(t) = \int_{-\infty}^{\infty} S_\theta(w) |w| e^{j2\pi w t} dw \quad (7)$$

Finally, the backprojection is performed to produce the reconstructed image. In this step, each pixel in the image is determined by the contribution of all filtered projections. Equation 8 shows the relationship between the filtered projection data  $Q_\theta(t)$  and the original function  $f(x,y)$ .

$$f(x,y) = \int_0^\pi Q_\theta(t) d\theta = \int_0^\pi Q_\theta(x \cos \theta + y \sin \theta) d\theta \quad (8)$$

The output of the reconstruction algorithm is a digital image composed of discrete picture elements, or pixels. As resolution increases and pixel sizes become smaller, the discrete image becomes a closer approximation of the continuous object it represents. Each pixel, usually of square dimensions, is assigned a discrete value representing the value of the function in a particular region. The elements in CT images are sometimes

referred to as voxels, or volume elements, because the CT slice represents a finite thickness determined by the X-ray beam and detector aperture. Thus, voxels represent discrete three-dimensional subvolumes of the object being imaged. Additionally, CT images may also be interpreted as a two-dimensional array of intensities mapping the distribution of linear attenuation coefficients for an object.

X-ray CT images come in a variety of formats, but the most popular are grayscale images 8–16 bits in size. The bit size of an image is related to the number of gray levels possible in the image. The formula that determines these values is  $(2^n - 1)$ , where  $n$  is the bit size of the image. Therefore, 8-bit images can have pixel values ranging from 0 to 255, with 0 corresponding to black, pixels with a value of 255 displaying as white, and values in between scaling linearly. Image file formats also vary, but lossless formats such as the TIFF (tagged image file format) standard are preferred so as not to lose any pixel information through file compression.

**1.4. Partial Volume Effect.** As mentioned previously, the pixels (or voxels) of a CT image represent a discrete subset of the object that is imaged. When the object is composed of a variety of different materials, each with its own characteristic X-ray attenuation properties, it is inevitable that some pixels will subtend material boundaries, and the CT values in such pixels will be some average of those attenuation properties. This phenomenon is known as the partial volume effect. Furthermore, the resolution that X-ray CT scanners can attain is limited, and material boundaries tend to be blurred. As a result, the CT value in any one pixel can be affected by material present in adjacent pixels.

When the CT values of the materials present are similar, a simple mixing-rule type calculation produces a reasonable estimate of the fraction of each material present. The orientation of the interface with respect to the scan plane also has an effect on the accuracy of this method. Additionally, the linear combination of attenuation characteristics weighted by volume fraction cannot determine the spatial distribution of the materials within a pixel. The partial volume effect can also result from temporal inconsistencies. The material in a subvolume described by a particular voxel can change composition during the course of CT data acquisition, in this study due to fluid flow. As a result, the grayscale assigned to that voxel will be based on a time-weighted average of the attenuation properties, depending on which materials were present and for how long. Typically in flow systems with small features, the partial volume phenomenon is observed as a combination of both temporal and spatial components. Notwithstanding this perceived limitation, quantitative data can be extracted by taking advantage of the partial volume effect. This theoretically permits measurement of features smaller than the pixel dimensions of the images, which is particularly important when considering small-scale features of an operating vapor-liquid packed column like packing sheet and liquid film thicknesses. Thus, it forms the basis for the calculations of void fraction and liquid holdup that this work explores.

## 2. Experimental Equipment and Operation

**2.1. X-ray Scanner.** The scanner used for the imaging experiments was located at the General Electric Quality Technology Center in Cincinnati, Ohio. This system, known as the industrial computed tomography (ICT) scanner, is used primarily for quality assurance from the neighboring General Electric Aircraft Engine plant. The imaging system consisted of measurement equipment to obtain the projection data and





**Figure 3.** Air–water column mounted on GE X-ray CT scanner with X-ray source, precollimator, and detector array visible.

**Table 1. X-ray CT Scanner Specifications**

|                             |                    |
|-----------------------------|--------------------|
| X-ray scanner               | GE                 |
| X-ray source maximum energy | 6000 kV            |
| detector type               | scintillator       |
| number of detectors         | 1024               |
| detector aperture           | 1.5 mm (0.059 in.) |
| maximum object weight       | 227 kg (500 lbs)   |
| maximum object diameter     | 1.02 m (40 in.)    |
| maximum scan height         | 0.97 m (38 in.)    |
| maximum object height       | 1.22 m (4 ft)      |

reconstruction and analysis software to produce and refine images. The GE scanner is a true-third-generation machine. The key features of the scanner are given in Table 1. The object being imaged is rotated rather than the source and detectors.

The GE scanner consists of a Varian Linatron linear accelerator X-ray source capable of producing a maximum X-ray energy of 6000 kV, or 6 MeV, but the scanner is typically operated with source energies of 2 or 6 MeV. Both of these values were used for the imaging studies contained in this work, with 6 MeV predominating. The beam is conical in shape but is collimated to a fan inside the source by two lead blocks. The beam passes through an adjustable precollimator where the slice thickness is set prior to reaching the object. Figure 3 depicts the GE scanner with the air–water column mounted for imaging.

The GE scanner's detector arrangement is a 1 m long linear array of 1024 ceramic scintillator detectors placed consecutively along an arc without gaps. The detectors are digital, meaning they are solid-state devices that convert incident X-rays directly to numerical values without the need for additional optical equipment. A computer then records the projection data. The detector aperture is fixed at 1.5 mm (0.059 in.). Each detector has a thin tungsten plate on each side to reduce cross-talk between detector elements. The object being imaged is attached to a computer-controlled manipulator capable of moving the object in 8 different axes. The source and detectors are both connected to a large overhead beam that is raised up and down

to the scan plane of interest. Measurement sensors are present to ensure precise locating of the object.

The computer system used in the GE scanner consists of a Hewlett-Packard computer and several networked hard drives for data storage. The filtered backprojection algorithm is used to reconstruct images. The software and data manipulation procedures used by GE are highly proprietary. The form of output is a 16-bit unsigned integer format, which can be converted to 16-bit TIFF images.

**2.2. Operating Procedures.** At start-up, measurements are performed at different conditions to calibrate the detectors. The first calibration records detector readings with the X-rays off to account for between-detector variations. Next, an air calibration with the X-rays turned on serves to determine the initial intensity of the X-ray beam, which is required to determine attenuation due to the object in subsequent scans.

The GE scanning procedure does not specifically require shift measurements to determine the center of rotation and position of the scan object in the fan beam at the start of a scan. However, the concept of shift is addressed by other calibration procedures performed periodically. The computer interface used to control the scanner includes commands to verify the manipulator is properly oriented to produce quality images. A jig may be attached to the turntable and imaged to adjust the scanning geometry parameters in the computer system. This procedure is known as CT-Center. Once CT-Center has been completed, a metal bowl that has been precisely milled to different radii is scanned. The operator confirms the size of the bowl by measuring the CT images; if the measurement from CT images agrees with the known physical dimensions of the bowl, then the scanner has been calibrated. This procedure is typically required after the manipulator and computer system suffer any communication errors.

**2.3. Air–Water Contactor.** The air–water column used for the imaging studies, shown in Figure 4, was developed during the work of Cartmel<sup>6</sup> and Schmit.<sup>7</sup> The clear acrylic column consists of three sections, each with an outer diameter of 15.24 cm (6 in.) and an inner diameter of 14.61 cm (5.75 in.). The sections are 15.24, 45.72, and 60.96 cm (6, 18, and 24 in.) in height and have flanges on both ends used for connecting the sections together. The bottom flanges of the 18 and 24 in. sections contain a groove designed to hold an O-ring, providing a watertight seal. The 6 in. section has a groove on both flanges.

The acrylic sections are connected together and attached to an 8.89 cm (3.5 in.) tall aluminum base. There are two process connections on the base, one for liquid flow out of the column and the other for vapor flow into the contactor. The column base is simply clamped to the turntable. Four stainless steel support rods are fed through holes on the flanges of the column sections and threaded into the base to provide additional mechanical stability. A schematic of the column is provided as Figure 5.

The lower section of the column contains the packed bed and the vapor distributor. The inverted cone-type vapor distributor has a base diameter of 11.43 cm (4.5 in.) and tapers to a 1.27 cm (0.5 in.) tubing connection that attaches to a 1.27 cm (0.5 in.) Swagelok fitting inside the column base. The base of the cone is covered with a perforated plate.

Several types of structured packing were used in the air–water contactor for imaging experiments. Initially, two 20.32 cm (8 in.) tall elements of Sulzer Mellapak 500Y ( $a_p = 500 \text{ m}^2/\text{m}^3$ ,  $\epsilon = 0.975$ ) stainless-steel structured packing were installed in the column. Sulzer Mellapak is a corrugated-sheet structured packing. The metal sheets are perforated to help



Figure 4. Acrylic air–water column used for imaging experiments.

equalize radial pressure profiles in the packing element and to promote liquid spreading. The surface of the packing is also textured to enhance spreading of the liquid. Wire gauze strips called wiper bands are wrapped around the circumference of the element and bent toward the column wall prior to installing the packing. These help direct liquid flow back into the packing element and prevent vapor channeling. The Y designation means that the angle of corrugation with respect to the horizontal is  $45^\circ$ .

To improve the liquid distribution, half elements of 500Y were tested in the contactor. The packing was constructed of the same material, but at 10.16 cm (4 in.) tall was half the height of the original packing. It is believed that the interface between two packing elements acts as a liquid redistributor. To address different liquid flow patterns, a sample of lower surface area Mellapak 250Y ( $a_p = 250 \text{ m}^2/\text{m}^3$ ,  $\epsilon = 0.987$ ) was installed in the column. Both full and half elements of this packing were tested. All structured packing elements in this work were installed  $90^\circ$  with respect to the previously installed element. The total height of packing for all Mellapak studies was 40.6 cm (16 in.). The liquid flow rates used for the experiments were 5.4, 25.7, 36.7, and  $48.9 \text{ m}^3/(\text{m}^2 \text{ h})$  (2.2, 10.5, 15.0, and  $20.0 \text{ GPM}/\text{ft}^2$ ). Vapor rates were F-factors of 0.33, 0.59, 0.79, 1.00, 1.22, 1.59, 1.71, and  $1.83 \text{ Pa}^{0.5}$  [ $0.27, 0.48, 0.65, 0.82, 1.00, 1.30, 1.40$ , and  $1.50 \text{ (ft/s)(lb}_m^{0.5}/\text{ft}^{1.5})$ ]. The vapor F-factor is defined as the product of the superficial vapor velocity and the square root of the vapor density,  $u_{s,v}\sqrt{\rho_v}$ . Figure 6 shows the packing types used in the imaging studies.

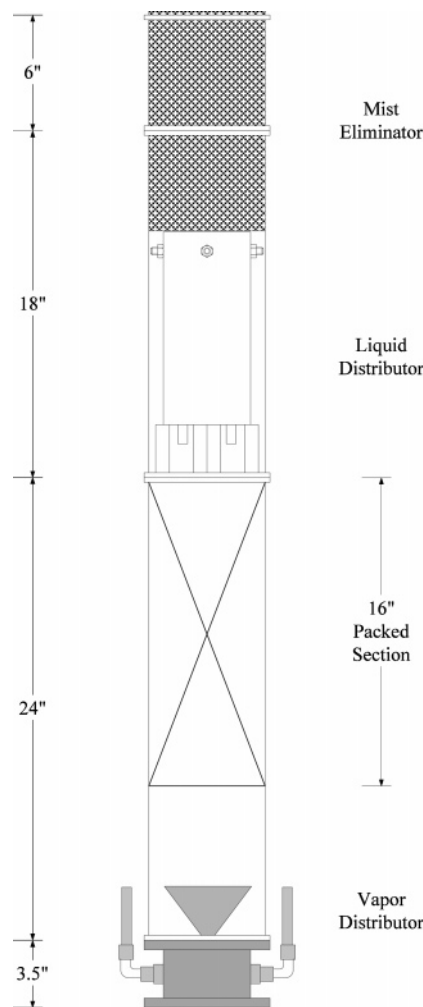


Figure 5. Schematic of the 15.2 cm (6 in.) air–water contactor used for X-ray imaging experiments.

**2.4. Flow System.** Modifications were made to the existing equipment setup to accommodate the unique challenges presented at the GE Quality Technology Center. The initial scans using the GE scanner used the in-house air supply. However, the flow was not sufficient to operate the contactor at industrially relevant vapor rates. Therefore, a diesel compressor was obtained for subsequent experiments. The GE scanner flow system equipment is shown in Figure 7.

The existing air flow meter was mounted to a cart along with the stainless steel tubes connected to the inlet and outlet. A second Micro Motion Basis F050 mass flow meter was installed on the cart to provide measurement of the liquid flow. The flow meter was wired to the existing data acquisition card and the LabVIEW code was adapted to display and totalize both air and liquid flow.

The liquid delivery system was designed for a recycle configuration using a Price model CD100AI centrifugal pump paired with a model M1105SC variable-frequency drive from AC Tech. This combination allows the pump speed and, thus, the flow rate to be controlled from outside the X-ray scanning bay. By adjusting the amount of liquid in the system via a bleed valve, a steady-state liquid level is held in the bottom of the column below the vapor distributor. The liquid is pumped out of the bottom of the column, through the water flow meter, and back into the top of the column. The larger pump required the liquid lines to be resized. The majority of the flexible vinyl tubing for water is 3.18 cm (1.25 in.) o.d., 2.54 cm (1 in.) i.d. However, this tubing is not as flexible as the smaller tubing.



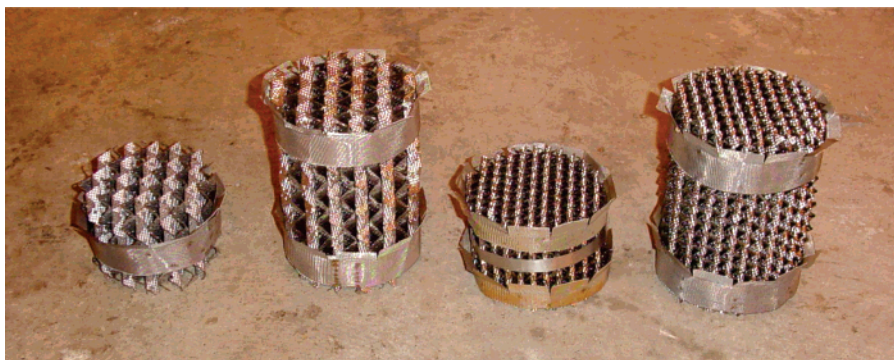


**Figure 6.** Structured packings used in the imaging studies: from left, Mellapak 250Y half element, 250Y full element, 500Y half element, and 500Y full element.



**Figure 7.** Flow system used with GE X-ray CT scanner: from left, air–water column, water pump, and cart containing flow meters. On top of the cart is the laptop computer and pump drive controller.

The larger hose was not ideal during the rotation of the column on the scanner. Thus, a short section of the original 1.91 cm (0.75 in.) o.d. tubing is used for the feed line to the liquid distributor. The mist eliminator was also improved to help prevent liquid entrainment at the higher vapor rates. A 22.86 cm (9 in.) tall bale constructed of a stainless steel and Teflon coking was obtained from ACS Separations & Mass Transfer Products. The distributor feed tube was routed through the middle of the mist eliminator and inserted into the distributor.

A liquid distributor was designed by Koch–Glitsch and utilized drip tubes to ensure that liquid head was maintained in the distributor for flow rate assurance. The drip tubes have a series of holes drilled at various heights to achieve the desired range of flow rates. The process flow diagram is shown in Figure 8.

### 3. Experimental Results and Discussion

**3.1. Image Acquisition.** The experiments began by imaging the packed section of the column at 2.54 cm (1 in.) intervals under conditions of zero vapor and liquid flow for a total of 16 horizontal slices. An example of a dry image is shown in Figure 9.

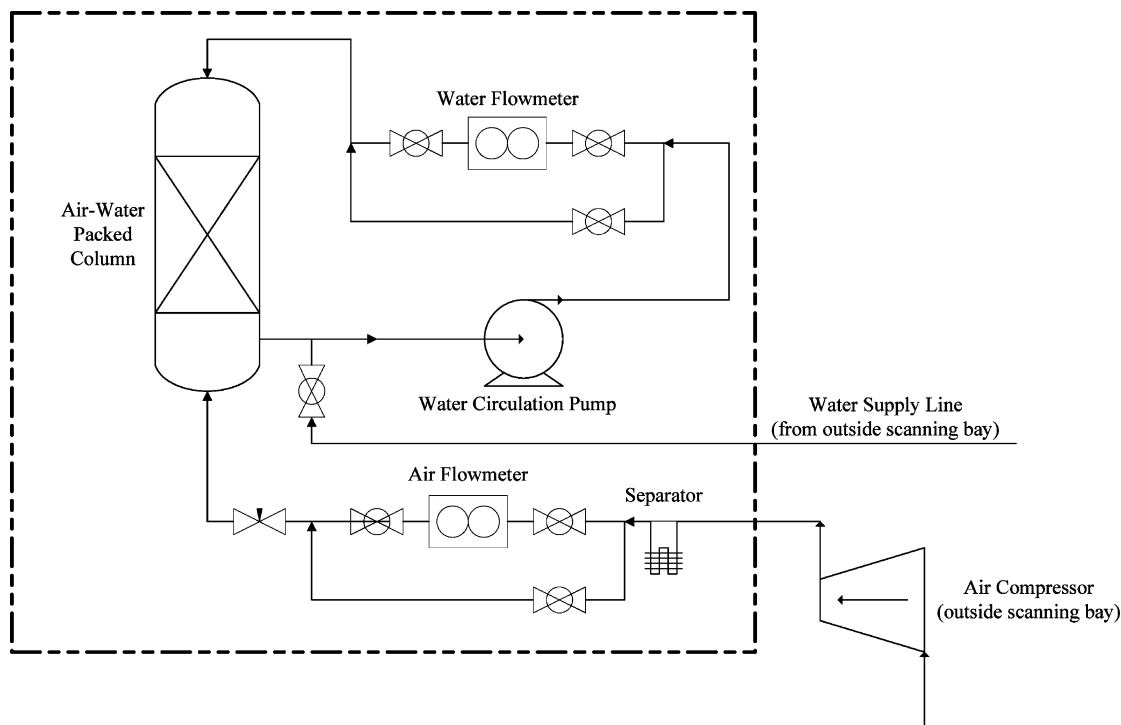
The edges of the metal support rods are very distinct. At this elevation, perforations are apparent on several of the corrugated sheets. The wiper band around the perimeter of the packing is also apparent in the image. The contact points between adjacent sheets are brighter because of a combination of static holdup remaining from the column leak test and the partial volume effect of a greater local metal fraction.

The column was then filled with water to observe the grayscale variation that could be expected during flow scans. Such an image is shown in Figure 10. The grayscale value of water was similar to that of the column wall, but the two phases can be differentiated visually. The overall grayscale intensity of the packing is brighter in the flooded image because of a partial volume effect, as the regions around the thin metal packing now contain water rather than air. The true end-member gray value for the packing, or the value that it would have were it thick enough to avoid edge effects, is expected to be comparable to the stainless steel posts outside the column.

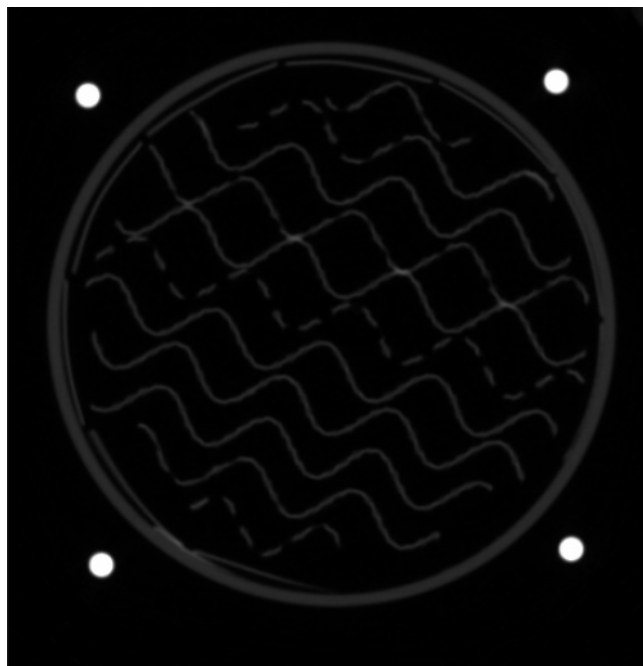
The column was then operated at several liquid and vapor rates while CT images were acquired for 16 horizontal slices in the packed region. Figure 11 shows a flow image for a liquid rate of  $36.7 \text{ m}^3/(\text{m}^2 \text{ h})$  (15.0 GPM/ft<sup>2</sup>) and a vapor F-factor of  $0.33 \text{ Pa}^{0.5}$  [ $0.27 \text{ (ft/s)(lb}_m^{0.5}/\text{ft}^{1.5})$ ]. The image represents a very distinct picture of the location of liquid, which can easily be identified on the surface of the packing sheets. Liquid does not appear in the flow channels, but some regions of water are present near the column wall.

Figure 12 shows the liquid films on the packing surface. The image grayscales have been adjusted to highlight the features. At this relatively high liquid rate, a large amount of water should be detectable throughout the packed section. Since the flow channels continue to remain as dark as they were in the dry images, it can be reasoned that the liquid flows as a film on the surface of the corrugated sheets. Regions of moderately light pixels appear on either side of the packing sheets. A well-defined meniscus is visible in the troughs of the corrugations, and liquid is observed to spread from one sheet to another at the contact points. The high surface tension of water is likely contributing to these phenomena. In the extreme of this case, potential area for mass transfer is being lost as the films are “pulled up” off the packing by surface tension forces.

In an image subtraction, the grayscale values of corresponding pixel locations in two different images are subtracted and mapped to the same pixel location in a new image. Therefore, it is critical that the object is oriented exactly the same in both source images to quantitatively measure the difference that can be attributed to flow in the application of CT imaging to packed columns. The quality of the CT image permitted image subtractions that clearly show the differences between dry CT slices and slices obtained under vapor and liquid flow. The pixels in the subtracted images could be classified as being air, water, or a combination of the two phases. An example of a subtracted image based on GE scanner data is shown in Figure 13. The liquid flow applied was  $36.7 \text{ m}^3/(\text{m}^2 \text{ h})$  (15 GPM/ft<sup>2</sup>), and the vapor F-factor was  $1.59 \text{ Pa}^{0.5}$  [ $1.30 \text{ (ft/s)(lb}_m^{0.5}/\text{ft}^{1.5})$ ].



**Figure 8.** Process flow diagram for air–water column. Heavy dotted line indicates scanning bay containment wall.



**Figure 9.** Sample dry CT image of Mellapak 250Y.

The subtraction image clearly shows that the liquid flows as films on the surface of the packing sheets, as seen by the shape of the water regions. Near the right side of the column, there is some flow off the packing sheets into the flow channels. Liquid branching near packing contact points is evident. The films appear to be thickest near the contact points, although the brighter appearance can also be a result of partial volume effects with greater local metal fraction. Some wall flow is visible in the lower-left portion of the column. Bright regions in the image exist where water was flowing for a long period during the scan. Lighter-colored regions define locations where the liquid flowed for only a portion of the scan or pixels where the liquid volume was small. Although the image is a time-averaged representation

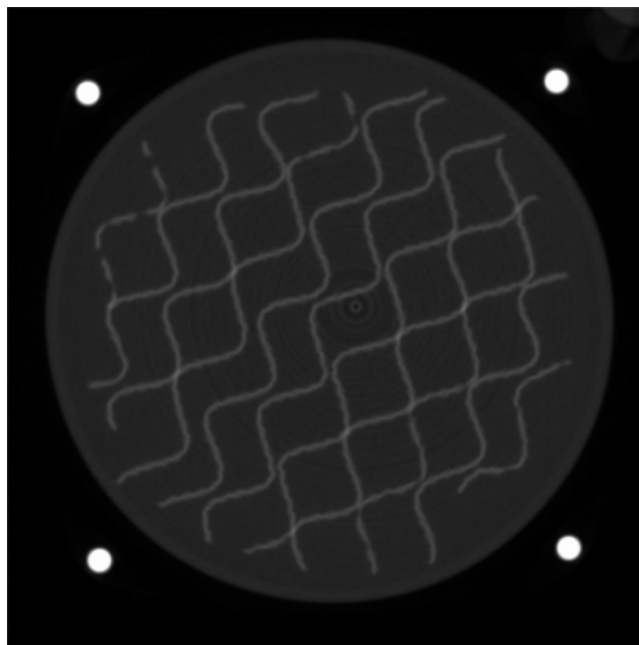


**Figure 10.** Flooded CT image.

of the flow, it provides some insight about the preferred flow pattern for the liquid under the flow conditions specified. Differences in film thickness and surface coverage can be seen in Figure 14, where subtractions of 5.4 and 36.7 m<sup>3</sup>/(m<sup>2</sup> h) (2.2 GPM/ft<sup>2</sup> and 15 GPM/ft<sup>2</sup>) are shown side by side. The air rate was an F-factor of 1.22 Pa<sup>0.5</sup> [1.00 (ft/s)(lb<sub>m</sub><sup>0.5</sup>/ft<sup>1.5</sup>)]. The flexible vinyl hose outside the column region is not resolved because of movement of the hose during the scan.

**3.2. Void Fraction and Liquid Holdup Determination.** By analyzing the pixel grayscale values in the 2-D CT slices, the void fraction of dry packing and liquid holdup in irrigated packing were calculated. The first step in processing the images is to determine the characteristic grayscale values for each of the phases present in an image. Since the analysis was limited



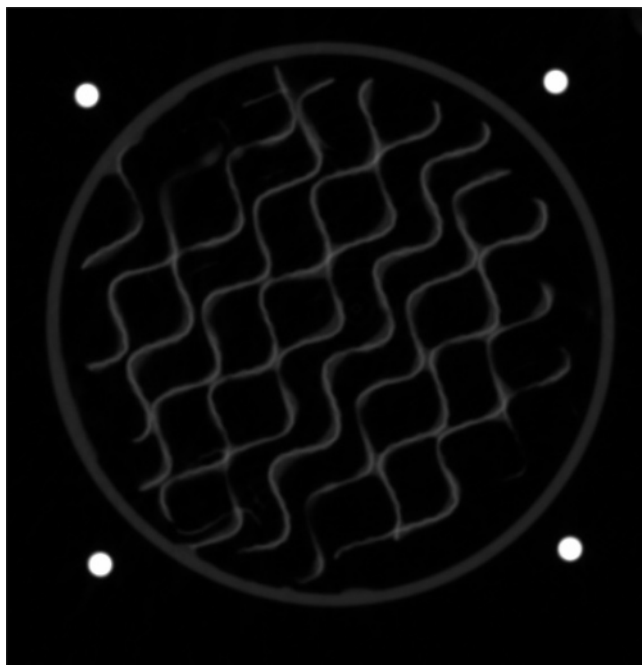


**Figure 11.** CT image of the flow field. Liquid rate is  $36.7 \text{ m}^3/(\text{m}^2 \text{ h})$  (15.0 GPM/ft<sup>2</sup>), and vapor F-factor is  $0.33 \text{ Pa}^{0.5}$  [ $0.27 \text{ (ft/s)(lb}_m^{0.5}/\text{ft}^{1.5})$ ].

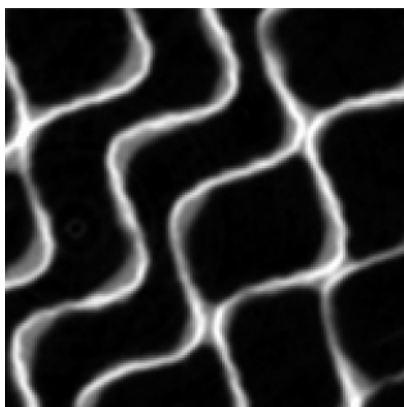


**Figure 12.** Water films on surface of Mellapak 250Y. Liquid rate is  $36.7 \text{ m}^3/(\text{m}^2 \text{ h})$  (15.0 GPM/ft<sup>2</sup>), and vapor F-factor is  $0.33 \text{ Pa}^{0.5}$  [ $0.27 \text{ (ft/s)(lb}_m^{0.5}/\text{ft}^{1.5})$ ].

to the column interior, the phases possible were air, water, and packing (steel). Image histograms were used to determine the most likely value for each phase. Figure 15 is a portion of a histogram for CT images from the GE scanner.

The histogram has been cropped to the region of interest. Each peak exhibits a normal distribution for a pure material. At the left edge of the image, the plot spikes to a very large number of pixels representing air. An air calibration is performed prior to the scans to set the attenuation of air as the baseline value, which forces a distribution centered at approximately zero. Since grayscales cannot be negative, the number of pixels with a value of zero will be higher as negative values are remapped to zero. In the flooded image, the large peak centered at a value of  $\sim 580$  primarily represents water and the column wall, with the metal packing being responsible for the apparent positive skewness. In both the dry and flow images, a smaller peak is observed at nearly the same region, primarily reflecting the column wall and the metal packing, with the latter having shifted to lower grayscale values because of the partial volume effect (i.e., spatial averaging with air rather than water). The slightly broader peak in the dry histogram is primarily due to the imperfect overlap between column wall and metal packing gray

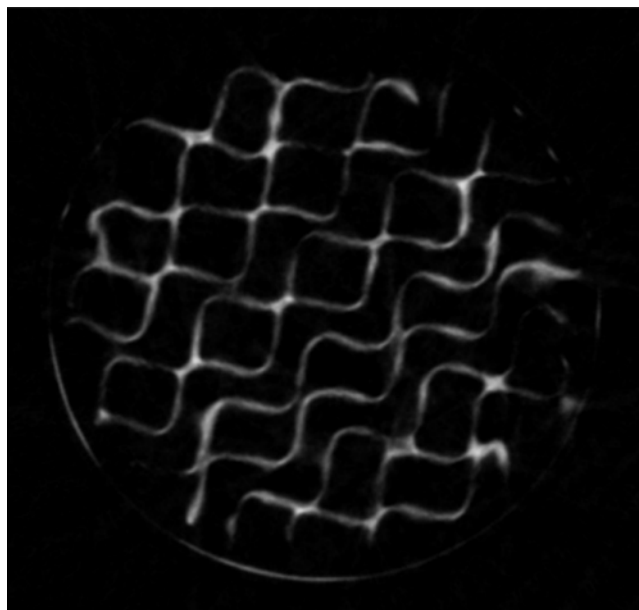


**Figure 13.** Subtraction image from CT data. Liquid rate is  $36.7 \text{ m}^3/(\text{m}^2 \text{ h})$  (15.0 GPM/ft<sup>2</sup>), and vapor F-factor is  $1.59 \text{ Pa}^{0.5}$  [ $1.30 \text{ (ft/s)(lb}_m^{0.5}/\text{ft}^{1.5})$ ].

values; in the flow image, the partial averaging of metal packing and some water has brought these peaks into closer congruence. The dry and flow images contain a greater number of pixels in the grayscale region from approximately 100 to 500. The pixels in this grayscale region represent an averaging between air and some other material. When the column is filled with water, there are fewer air–material interfaces. Because of variances in air conditions and X-ray source energy, the characteristic grayscale values for each material can vary from scan to scan.

Since the grayscale value of a pixel filled with metal packing cannot be determined because of the packing sheets being thin, an estimation of the grayscale value of a metal-filled pixel is required. The stainless steel struts outside the column region provide a good estimate which can then be fine-tuned to produce a void fraction value close to the vendor-specified figure. To verify the value assumed for the strut region, packing sheets were extracted from a surplus packing element, stacked, hammered flat, and folded to occupy more than 1 pixel of space. The sheets were attached to the side of the column during a scan and analyzed in the images to determine the characteristic grayscale. For pixels in the image that constitute the interior region of the column where only metal and air are expected during dry scans, the grayscale value of each pixel is divided by the chosen characteristic grayscale for metal packing. This determines the fraction of a pixel (or voxel) attributable to packing, although in reality, the blurring aspect of X-ray CT causes some signal bleed, resulting in pixels that possess a grayscale higher than pure air yet contain no metal. Summing the fractions over the entire column area of pixels and dividing by the total column area determines the metal fraction. The sum of the metal fraction and void fraction will equal 1 in a completely dry image.

A separate method for identifying grayscale values involves drawing a line across the image and plotting the grayscale value of each pixel along the line. This is known as a line profile. Additional information can be gathered for the measurement of features in the image relative to the size of a pixel. One specific example is evaluating the difference in grayscale between dry and flow images by investigating the edge response function along a line that passes across packing sheets. Figure 16 is an example of line profiles drawn in dry and flow images,

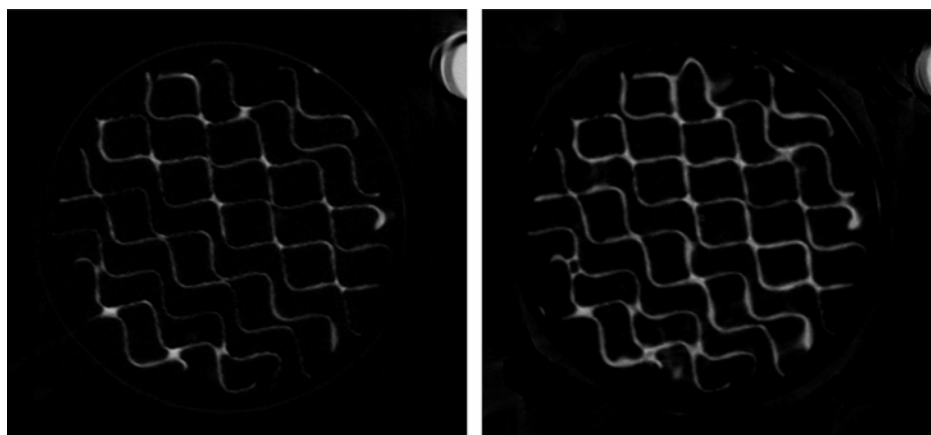


**Figure 14.** Difference images for liquid flows of  $5.4 \text{ m}^3/(\text{m}^2 \text{ h})$  ( $2.2 \text{ GPM}/\text{ft}^2$ ) (left) and  $36.7 \text{ m}^3/(\text{m}^2 \text{ h})$  ( $15.0 \text{ GPM}/\text{ft}^2$ ) (right) at an F-factor of  $1.22 \text{ Pa}^{0.5}$  [ $1.00 \text{ (ft/s)}(\text{lb}_m^{0.5}/\text{ft}^{1.5})$ ].

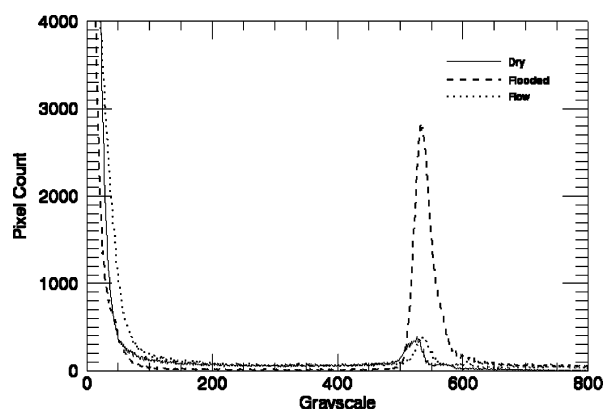


**Figure 15.** Histogram of three images representing different flow conditions for structured packing.

with both the images and the grayscale response shown. The lines are shown in red on the CT images.

The profile through the stainless steel support rod appears the same in both the dry and flow line profiles. The grayscale response forms a plateau at the characteristic grayscale value of the bulk material. Near the edges, the response drops off sharply. A clear difference can be seen in the response for the line drawn through the water outlet hose. In the dry image, the hose is empty, and the response between the peaks for the hose wall is low. However, when the hose is full during the flow scan, the height of the plateau region defines the average grayscale of water. The characteristic grayscales for water and the vinyl wall of the hose are similar. The water grayscale is fairly constant across the tube. Finally, the response across the packing sheets is different for the flow and dry scans. In the dry profile, the peaks for water are shorter and narrower, indicating that a small amount of material is present. Because the grayscale value of metal packing is expected to be high, the reduced height of the packing peaks indicates that the packing is small compared to the pixel size. This phenomenon can also be attributed to the thickness of the packing compared to the point-spread function of the scan image, which defines the blurring radius that is apparent. The peaks do not exhibit a plateau, but instead resemble a spike. In the flow image, however, the packing peaks are higher and somewhat broader. This signifies that material that attenuates X-rays more than air was present in the region around the packing and added to the overall thickness in the region being considered. Quantification of the liquid film thickness by comparing the respective edge responses for the dry and flow cases is difficult because of the small fraction of water present compared to the size of a pixel.

Therefore, the line profiles are most helpful in determining the grayscales associated with particular regions in the column.

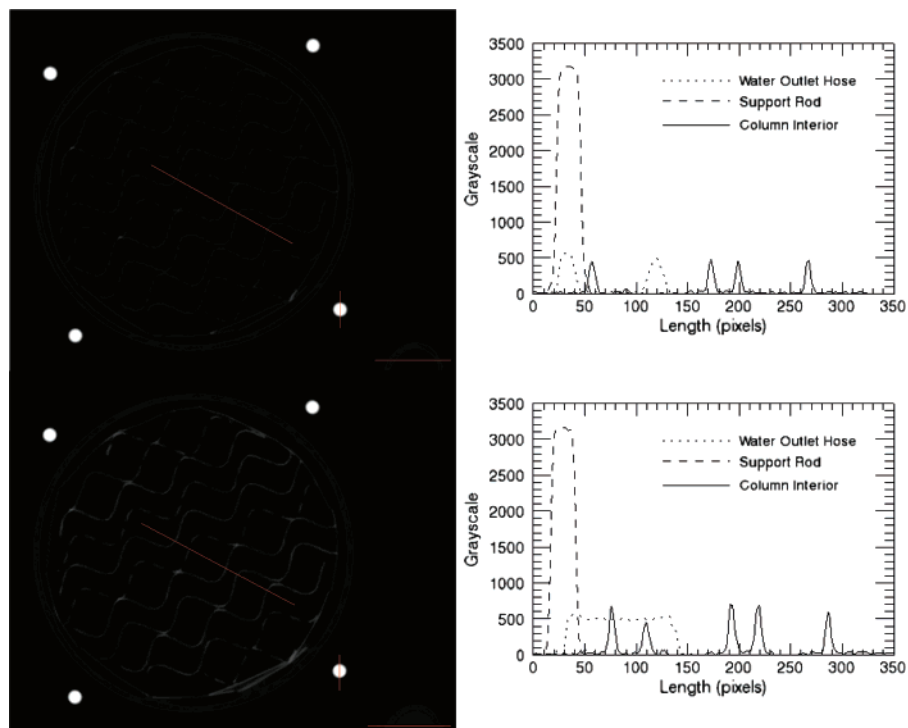
The local void fraction of dry packing and liquid holdup of the irrigated bed was evaluated for 16 slices through the packed section, spaced at  $2.54 \text{ cm}$  ( $1 \text{ in.}$ ) intervals. For reference, Figure 17 shows a radiogram of the column equipped with Mellapak 250Y half elements. The image has been marked to denote the relative elevation from the zero height point on the scanner turntable. The joint between packing elements can be identified by the small void space that spans the column diameter and by the change of packing sheet orientation.

Figure 18 shows the variation in void fraction with elevation in the packed bed along with the average from the 16 CT slices and the vendor-specified value. It is clear that void fraction is not constant throughout the bed. Factors that contribute to this behavior are the location of the scan plane in relation to perforations, wiper bands, and joint interfaces. The vendor-specified value does not account for wiper bands, which will cause the average true void to be lower. Additionally, the 16 slices throughout the bed may fall in locations that skew the average. For instance, if a slice is located at a packing element joint, the calculated void fraction will be higher than in the bulk of the packing.

In addition to observing behavior throughout the column, the packing element joint area was investigated further by taking a series of closely spaced CT slices near the interface of two elements. The total height scanned above and below the actual interface ranged from  $3.05$  to  $11.03 \text{ mm}$  ( $0.12$ – $0.45 \text{ in.}$ ) using slice spacings of  $0.76$  to  $1.27 \text{ mm}$  ( $0.03$ – $0.05 \text{ in.}$ ). A plot of void fraction versus elevation is shown in Figure 19. The horizontal line was determined to be the elevation where the actual interface was located. Portions of corrugated sheets from both elements were visible in CT images obtained at this elevation.

Difference images were created to analyze liquid holdup by subtracting the dry image from a flow image at the corresponding elevation. Applying the void fraction calculations to the water phase present in the column using the characteristic water grayscale provides the fractional amount of liquid at a particular location in the packed bed.

The holdup calculations were performed numerically using IDL software, which increased the throughput of data analysis. The first images acquired with the GE scanner were for moderate F-factors up to  $0.59 \text{ Pa}^{0.5}$  [ $0.48 \text{ (ft/s)}(\text{lb}_m^{0.5}/\text{ft}^{1.5})$ ]. As depicted in Figure 20, for liquid rates of  $5.4$  and  $25.7 \text{ m}^3/(\text{m}^2 \text{ h})$  ( $2.2$  and  $10.5 \text{ GPM}/\text{ft}^2$ ), the holdup was mostly independent of the gas rate, indicating that the column was still operating



**Figure 16.** Line profiles for dry (top) and flow (bottom) CT images. Liquid flow is  $25.7 \text{ m}^3/(\text{m}^2 \text{ h})$  ( $10.5 \text{ GPM}/\text{ft}^2$ ), and vapor F-factor is  $1.22 \text{ Pa}^{0.5}$  [ $1.00 (\text{ft}/\text{s})(\text{lb}_\text{m}^{0.5}/\text{ft}^{1.5})$ ].

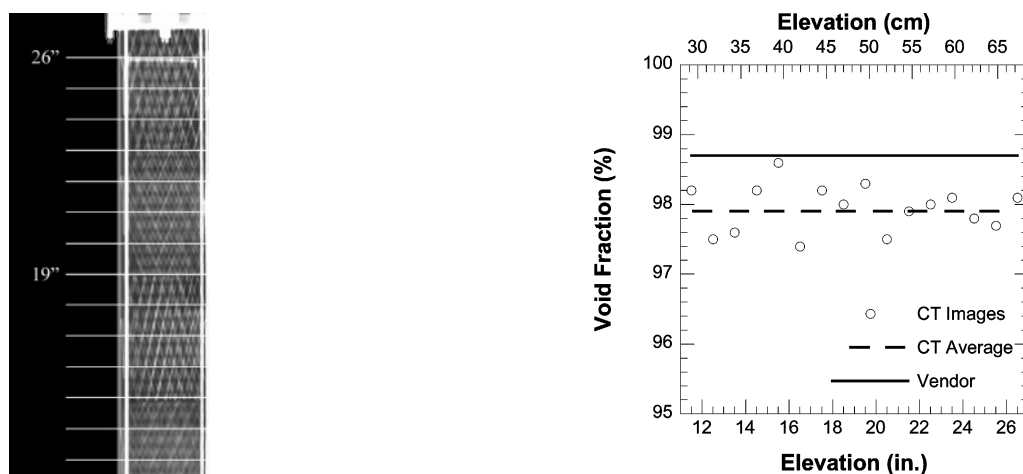


**Figure 17.** Radiogram with scan planes for bulk holdup and void fraction marked.

below the loading point. However, for a liquid rate of  $36.7 \text{ m}^3/(\text{m}^2 \text{ h})$  ( $15.0 \text{ GPM}/\text{ft}^2$ ), the holdup exhibited greater variation with respect to air rate. At the low vapor F-factor of  $0.33 \text{ Pa}^{0.5}$  [ $0.27 (\text{ft}/\text{s})(\text{lb}_\text{m}^{0.5}/\text{ft}^{1.5})$ ], the liquid holdup was similar to that calculated for a liquid rate of  $25.7 \text{ m}^3/(\text{m}^2 \text{ h})$  ( $10.5 \text{ GPM}/\text{ft}^2$ ), at least near the bottom of the column. At higher elevations, the holdup was higher, mirroring the data calculated for the F-factor of  $0.59 \text{ Pa}^{0.5}$  [ $0.48 (\text{ft}/\text{s})(\text{lb}_\text{m}^{0.5}/\text{ft}^{1.5})$ ]. At a lower vapor rate and higher liquid rate, the vapor drag forces on the falling

**Figure 18.** Void fraction profile in Mellapak 250Y structured packing.

liquid are low compared to the gravitational force acting on the liquid. The liquid is then able to drain unobstructed from the bed. As the vapor rate increases, however, the liquid will be held up in the packed bed by the vapor drag. The fact that the holdup at  $36.7 \text{ m}^3/(\text{m}^2 \text{ h})$  ( $15.0 \text{ GPM}/\text{ft}^2$ ) is similar for both air rates near the top of the column is likely a distribution issue. After  $\sim 10 \text{ cm}$  ( $4 \text{ in.}$ ), which is the height of one packing element, the holdup plots begin to deviate, suggesting a change in flow pattern as the first element interface is encountered.

Overall, local peaks are observed in the holdup plots. When elevation 15 is located in Figure 17, it is found to be located slightly above a packing element interface. Elevation 11 is located in the bottom of the bottom-most packing element, and near to the vapor inlet. Vapor entrance effects were noticeable during column operation using video cameras mounted in the scanning bay. Both vapor inlet considerations and joint behavior are likely to result in increased holdup as observed in Figure 20.



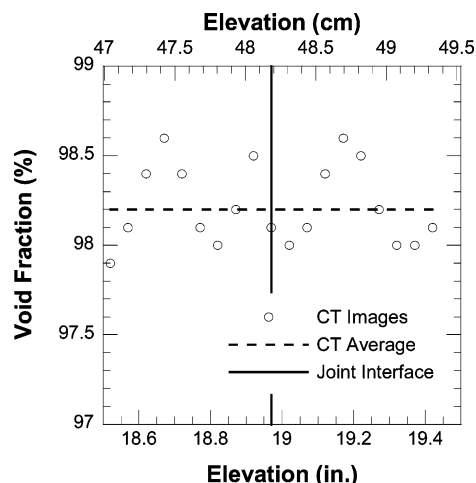


Figure 19. Void fraction in packing element joint region.

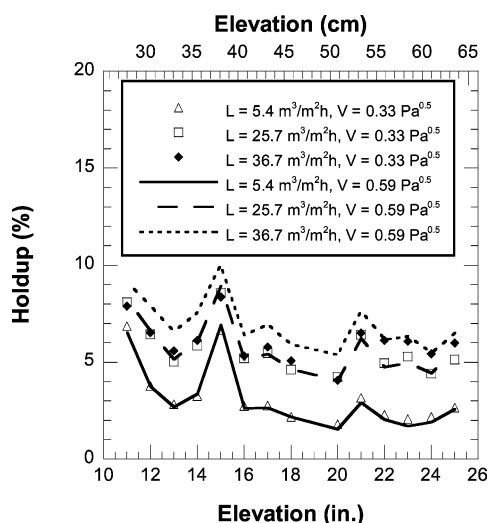


Figure 20. Liquid holdup as a function of elevation calculated from GE scanner images.

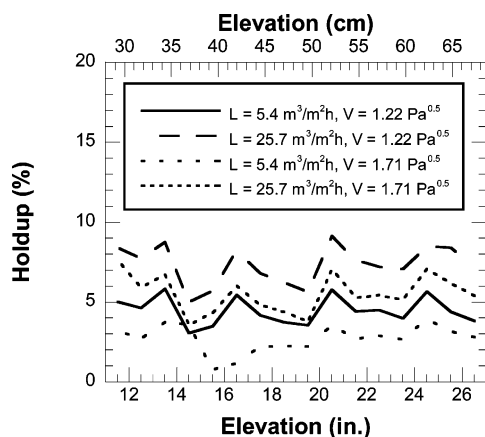


Figure 21. Liquid holdup versus elevation at F-factors of 1.22 and 1.71  $\text{Pa}^{0.5}$ .

At higher vapor rates, the holdup behavior becomes somewhat more erratic. In Figure 21, the liquid holdup throughout the column is shown for F-factors of 1.22 and 1.71  $\text{Pa}^{0.5}$  [1.00 and 1.40 (ft/s)( $\text{lb}_m^{0.5}/\text{ft}^{1.5}$ )] and two liquid rates. More variation is seen across the packed section, with fewer regions where the profile is relatively flat. The holdup is actually higher for both liquid rates at an F-factor of 1.22  $\text{Pa}^{0.5}$  [1.0 (ft/s)( $\text{lb}_m^{0.5}/\text{ft}^{1.5}$ )] compared to the data at F-factor 1.71  $\text{Pa}^{0.5}$  [1.40 (ft/s)( $\text{lb}_m^{0.5}/\text{ft}^{1.5}$ )]. This behavior is not expected.

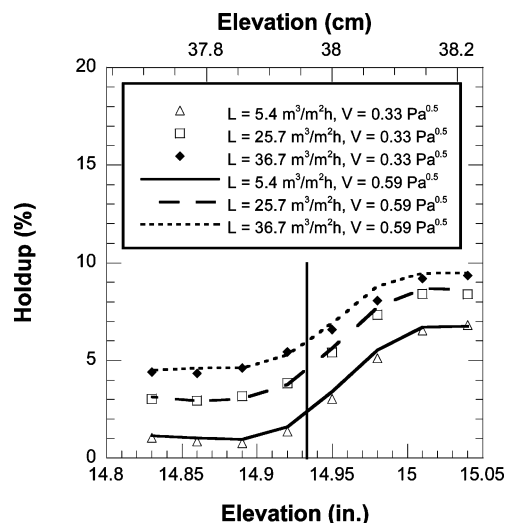
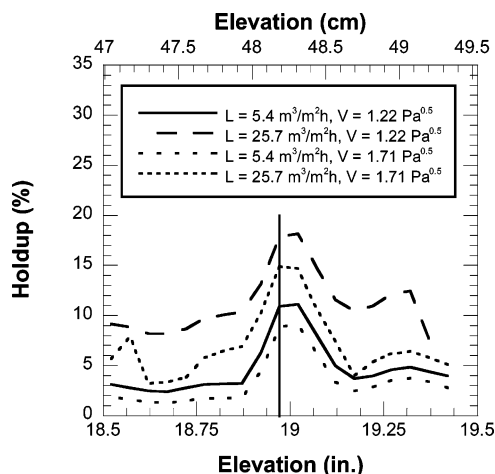


Figure 22. Liquid holdup at bottom packing element joint. Vertical line represents actual interface.

At a liquid rate of 5.4  $\text{m}^3/(\text{m}^2 \text{ h})$  (2.2 GPM/ $\text{ft}^2$ ) and an F-factor of 1.71  $\text{Pa}^{0.5}$  [1.40 (ft/s)( $\text{lb}_m^{0.5}/\text{ft}^{1.5}$ )], the overall holdup is comparably low. During operation at this rate, the bottom packing element was bordering on a flooding regime. The low liquid flow allowed material to be easily pushed back into the column by the higher vapor flow, creating a turbulent pattern in the bottom element. Such flow will not be resolved by the X-ray technique, as the characteristic time scales are very different. The flow will appear as a random assortment of pixels with grayscales determined by partial volume and partial time components in a time-averaged image. Near elevation 14, the holdup is a minimum for three of the rates. This corresponds to an area slightly below a packing joint. Liquid pooling at the interface above seems to impede the overall liquid progress through the bed. Poor overall distribution will result from accumulation in any one part of the column.

Local peaks in liquid holdup observed near packing joints were further investigated by calculating the holdup for closely spaced slices taken around element interfaces. Initially, a total of 8 slices were taken at 0.76 mm (0.03 in.) spacing resulting in a total height of 6.10 mm (0.24 in.). The holdup profiles at the bottom-most joint are shown in Figure 22. The vertical line represents the actual location of the interface. As was observed previously for these same flow rates, the holdup is independent of gas rate. Each condition exhibited higher liquid holdup above the joint, transitioning to a moderate value at the interface and tapering off as the liquid enters the bottom packing element. The apparent discontinuity in holdup from packing entrance to packing exit suggests that the holdup above the joint was actually a local maximum. Additional slices taken above and below the joint would provide additional insight to the expected pattern of holdup across an entire packing element.

The number of slices around the joint region was increased to 19 in subsequent scans of the middle packing joint at higher F-factors. The slice spacing was increased to 1.27 mm (0.05 in.). Holdup profiles for F-factors of 1.22 and 1.71  $\text{Pa}^{0.5}$  [1.00 and 1.40 (ft/s)( $\text{lb}_m^{0.5}/\text{ft}^{1.5}$ )] are shown in Figure 23. The behavior in the region that was shown previously in Figure 22 is very similar. Additional slices taken above the interface show that the high holdup at the joint is a local maximum, where the value of holdup ranges roughly from 2 to 5 times the value observed in the bulk of the element. The region of liquid accumulation extends approximately 6.4–10 mm (0.25–0.4 in.) above the interface of the elements. After passing into the next element,



**Figure 23.** Profile of liquid holdup at a packing element interface. Vertical line represents actual interface.

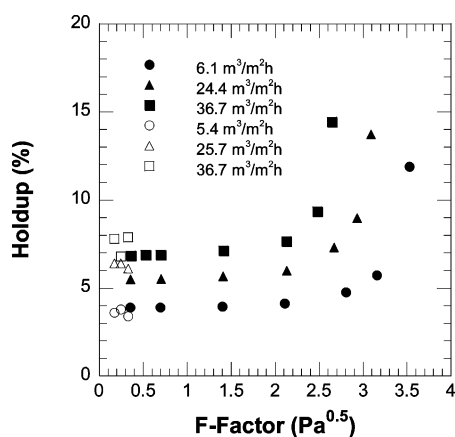


**Figure 24.** Experimental liquid holdup for Mellapak 250Y. Solid data markers represent 45.7 cm (18 in.) SRP column data, and open data markers were taken from 15.2 cm (6 in.) column used for X-ray experiments.

the holdup returns to a lower value. Similar to the bulk column holdup data at higher vapor rates, the liquid holdup appears to decrease with increasing F-factor. The data in Figure 23 was also obtained just prior to the GE X-ray scanner experiencing technical issues. Level shifts in the data sets could lead to such a phenomenon in the calculations.

To evaluate the validity of the holdup data calculated from X-ray CT images, traditional experimental methods for determining holdup were used. Both the 6 in. air–water contactor used for the imaging studies and the SRP 45.7 cm (18 in.) air–water column were used to determine the volume of liquid that drained from the packed bed after liquid flow to the column ceased at different flow conditions. In Figure 24, the results of experimental holdup measurements on the column used for imaging are compared with SRP data from the hydraulic testing of Mellapak 250Y. The experimental measurements on the smaller column were limited to low F-factors provided by the building nitrogen supply. The agreement with the large column data in the low range of vapor rates is acceptable. The general trend shows holdup to be independent of gas rate up to the loading point, and then increasing dramatically as the flood point is approached. A corresponding increase in overall column pressure drop would accompany the sharp upturn in holdup.

The traditional experimental techniques report the column average holdup, whereas image analysis provides a local value that has been shown to vary with elevation. Comparing the experimental values of liquid holdup to the values calculated from X-ray CT requires the data from images to be averaged

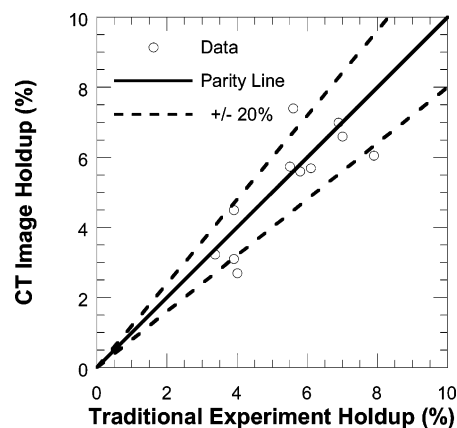


**Figure 25.** Parity plot comparing two experimental methods for predicting holdup.

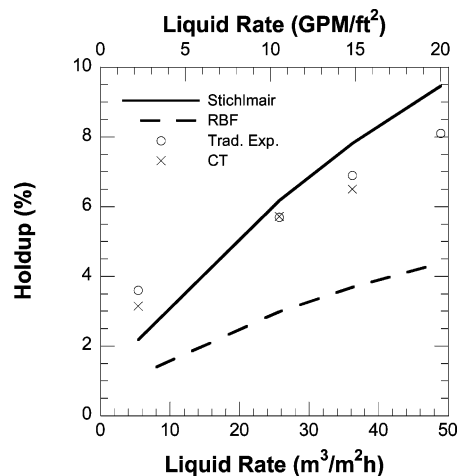


**Figure 26.** Comparison of traditional and X-ray experimental measurements of liquid holdup versus predictive models.

over the series of equally spaced slices to obtain an average holdup for the column. The average of the holdup values determined from CT images is not a true representation of the entire column, because relatively few data points were taken in relation to the column height, some of which fell in regions near joints known to deviate highly from the bulk flow. However, as seen in Figure 25, the agreement between the two methods generally falls within 20%. The traditional method of calculating holdup does not account for liquid that remains in the bed as static holdup, whereas the CT technique gives the total amount of liquid present in a slice, whether it constitutes static or dynamic holdup.

When the experimental data measured for holdup are compared to two existing models for predicting column performance, the strongest agreement exists between the two experimental techniques. Neither the Stichlmair model<sup>8</sup> nor the Rocha–Bravo–Fair model<sup>9,10</sup> predict liquid holdup close to the experimental values. It should be noted that all data in Figure 26 are below the loading point. Models for predicting hydraulic performance above the loading point are notoriously inaccurate, as the hydraulic parameters are tweaked or fit empirically to satisfy the mass transfer constraints. Both models underestimate the liquid holdup at low liquid rates. The Rocha–Bravo–Fair model consistently predicts values for holdup much lower than the experimental data showed, whether it was by traditional experiment or by CT image analysis. The Stichlmair model follows the general curve exhibited by the experimental data at intermediate liquid rates but begins to deviate from the data as higher liquid rates are encountered.

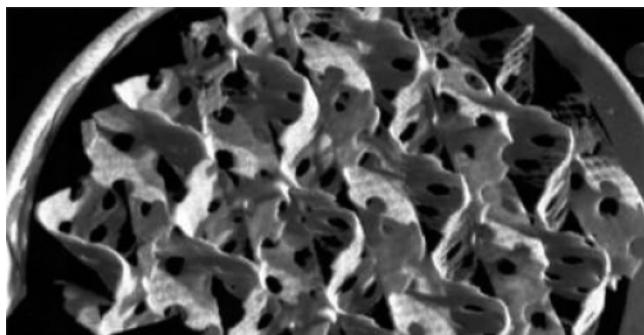


**Figure 27.** Three in. model of irrigated structured packing created from a series of CT slices. Liquid rate is  $25.7 \text{ m}^3/(\text{m}^2 \text{ h})$  (10.5 GPM/ft<sup>2</sup>), and vapor F-factor is  $0.59 \text{ Pa}^{0.5}$  [ $0.48 \text{ (ft/s)(lb}_m^{0.5}/\text{ft}^{1.5})$ ].



**Figure 28.** 3-D reconstruction of air–water column using a series of 2-D CT images.

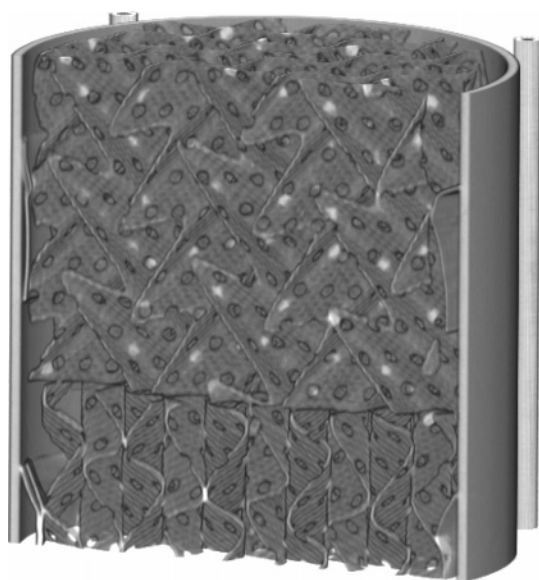


**Figure 29.** Cutaway view of air–water column containing structured packing.

**3.3. 3-D Reconstructions from X-ray CT Data.** With each X-ray CT slice being of finite thickness, a series of slices can be stacked to simulate a volume. As the slice thickness and spacing between slices decreases, the data set becomes a more accurate representation of the physical system. Volumetric

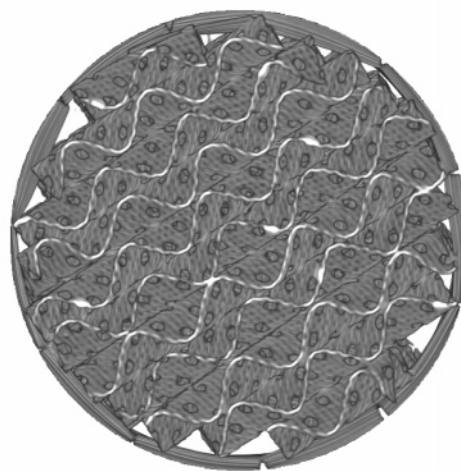
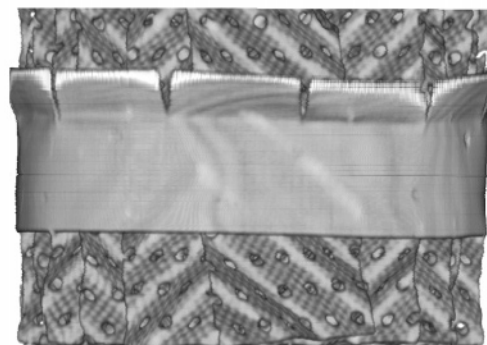


**Figure 30.** 3-D reconstructions of a Mellapak 250Y half element from X-ray CT data.

visualization of the packed bed under dry and flow conditions was possible using this approach. As with CT slices, the 3-D reconstructions of the column under flow conditions represent a time average of the flow behavior over the course of the scan.

Initially, a 7.6 cm (3 in.) section of structured packing at the top of the bed just below the distributor was modeled while a liquid flow of  $25.7 \text{ m}^3/(\text{m}^2 \text{ h})$  (10.5 GPM/ft<sup>2</sup>) and vapor F-factor of  $0.59 \text{ Pa}^{0.5}$  [ $0.48 \text{ (ft/s)(lb}_m^{0.5}/\text{ft}^{1.5})$ ] were applied. The first attempt at modeling was used to evaluate the technique; therefore, a corresponding dry model was not obtained. The



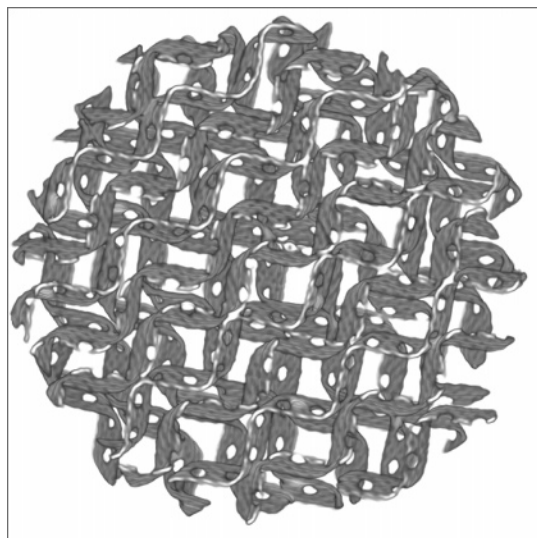


**Figure 31.** 3-D image of column cross section as a packing element joint is approached.

reconstruction shown in Figure 27 was provided by General Electric's image processing team.

The resolution of the X-ray CT scanner is sufficient to capture the surface texture and perforations of the packing sheets. Without a corresponding dry image to compare to, it is somewhat difficult to identify features that may be present due to flow. Also, since the model was obtained near the top of the bed, the liquid has not had ample time to distribute across the sheets. On the basis of this fact, it is presumed that the majority of the liquid is in the center of the column. One theory that has been discussed relates to the appearance of the surface texturing. Near the column walls, the surface treatment appears more pronounced than it does in the middle of the column. It would be expected that a film of liquid on the surface of the packing would obscure the surface texturing, resulting in a smoother appearance in a reconstruction of this type. However, the light source that has been applied to highlight the features of the packing may be contributing to this observation.

Subsequent experiments using the 3-D modeling technique employed both dry and flow models at identical locations in the packed column. Thus, a series of subtracted images could be obtained that corresponded to the same region. In theory, the subtracted images could also be stacked to create a model that included only the liquid flowing through the bed. Unfortunately, the modeling scans are very lengthy. For example, at a spatial resolution of 0.25 mm (0.01 in.) for both the pixel dimension and slice spacing, a 600-slice, 15.2 cm (6 in.) model takes approximately 10 h to obtain. Therefore it is critical to maintain precise control of the liquid and vapor flows to the column. The technique is currently unable to capture turbulent flow patterns such as those encountered as the flood point is approached. However, for cases where liquid films dominate at steady state, the reconstructions have shown some promise.

Using Amira, a three-dimensional data visualization software package, image stacks from subsequent modeling experiments were created. An example of such a reconstruction is shown in Figure 28. By manipulating the color table, noise and artifacts can be filtered out of the system and the features of interest, such as the packing, can be emphasized. The image shows a 15.2 cm (6 in.) tall section of the air–water column containing structured packing. As in the GE-provided image, the perforations and texture of the packing are apparent. Also visible in the image are the four steel column support rods, the acrylic

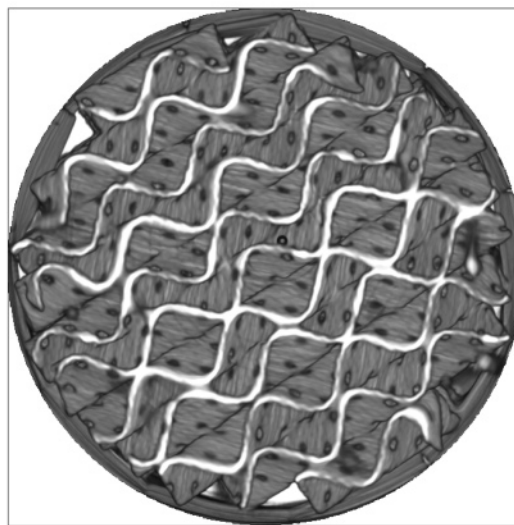
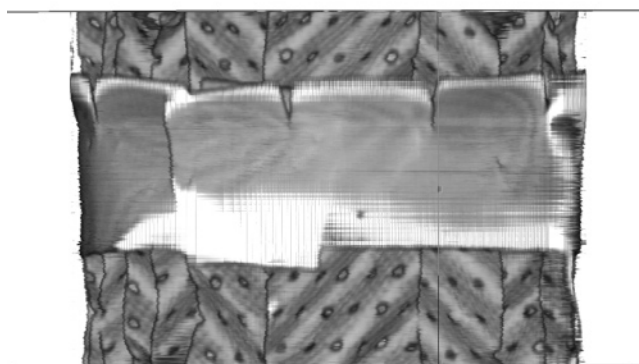
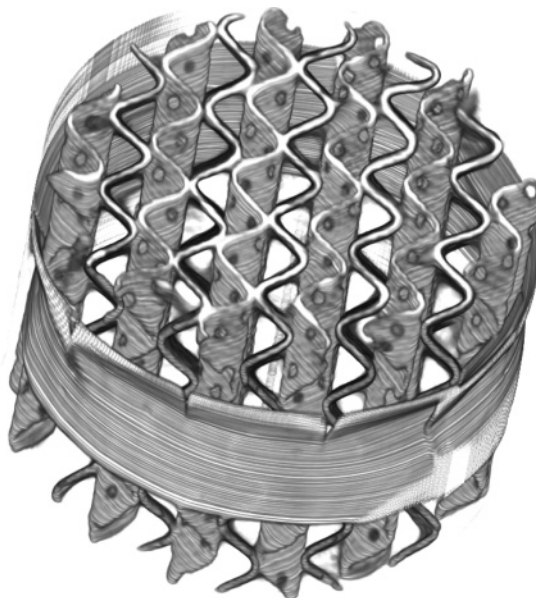


**Figure 32.** 3-D reconstructions of CT slices obtained under flow. Liquid rate is  $36.7 \text{ m}^3/(\text{m}^2 \text{ h})$  (15.0 GPM/ft<sup>2</sup>), and vapor F-factor is  $1.59 \text{ Pa}^{0.5}$  [ $1.30 \text{ (ft/s)(lb}_m^{0.5}/\text{ft}^{1.5})$ ].

column wall, and the water outlet hose, which is empty in this case. Bright spots in the packing signify regions of pixels where the metal fraction is higher, such as near the contact points of adjacent sheets.

A cutaway view of the column showing the packing interior is shown in Figure 29. The wiper bands surrounding the elements are visible between the packing sheets and the column wall. The change in packing sheet orientation from one element

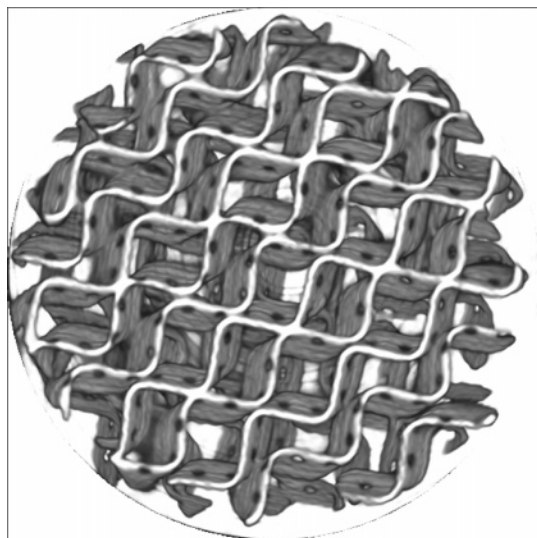


**Figure 33.** Packing element joint region under flow conditions. Liquid rate is  $36.7 \text{ m}^3/(\text{m}^2 \text{ h})$  ( $15.0 \text{ GPM}/\text{ft}^2$ ), and vapor F-factor is  $1.59 \text{ Pa}^{0.5}$  [ $1.30 \text{ (ft/s)(lb}_m^{0.5}/\text{ft}^{1.5})$ ].

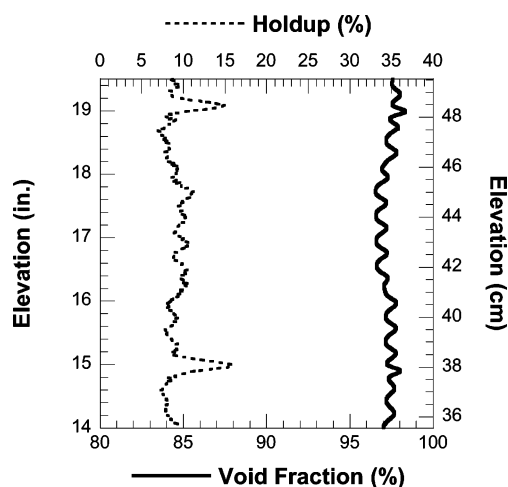


**Figure 34.** Void fraction and holdup profiles in a 14 cm (5.5 in.) tall section of packing. Liquid rate is  $36.7 \text{ m}^3/(\text{m}^2 \text{ h})$  ( $15.0 \text{ GPM}/\text{ft}^2$ ), and F-factor is  $1.59 \text{ Pa}^{0.5}$  [ $1.30 \text{ (ft/s)(lb}_m^{0.5}/\text{ft}^{1.5})$ ].

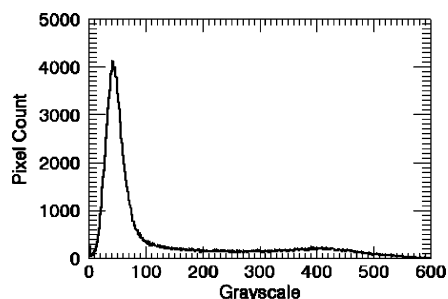


**Figure 35.** Histogram for CT image of dry structured packing, from which a threshold grayscale of 150 was chosen.

to the next can also be seen. Numerous bright spots are visible on the open side surface of the packing due to the cutaway procedure. These are areas where packing sheets are in contact when the volume is viewed as a whole. A distinct void is observable at the interface between the two packing elements. The grayscales associated with metal packing, metal support rods, and the acrylic wall are consistent, providing good differentiation among the materials present. The surface treatment and perforations can be examined in detail with this view.

The perimeter of the perforations appears smooth, indicating that the spatial resolution of the 2-D images and the slice spacing is adequate.

If the two-dimensional CT images are cropped prior to being read into Amira, the column wall, support rods, and hoses can be removed in order to focus on the packing elements themselves. Figure 30 provides several views of a packing element reconstructed from cropped CT images obtained from the dry bed. The flow channels are clearly visible in the angular view. The wiper band appears around the perimeter of the element, including the tabs that have been bent to provide a seal against the column wall. Portions of the wiper band are not resolved after the cropping procedure since they touch the column wall. Because of the partial volume effect and the related low grayscale value of packing in the CT images, the packing sheets appear thicker in the reconstructions than they are in reality. However, all other characteristics of the packing are to scale.

In the side view, the tack welds used to fasten the wiper band to the element are visible. The top-down view provides a look at how the fit of 250-series packing in a relatively small diameter column can emphasize wall effects. A large amount of void space can be seen in the upper- and lower-left portions of the image.

With the joint region of packing producing interesting results for liquid holdup from 2-D slices, a 3-D reconstruction of the column cross section near a packing element joint was created for volume visualization. Seen in Figure 31, the overhead image shows how packing sheets from the lower element are visible through the flow channels of the upper element. As the total height of column viewed in this manner is decreased, the apparent void space will increase. The path for liquid flow from one element into the next is clearly nonideal. Films falling off of sheets in the upper element are fed directly into void space in the lower element. Rising vapor in the flow channels interacts with this liquid, which must change direction sharply. This bottleneck serves as a likely point for flooding to begin.

Reconstructing 3-D models using CT slices obtained while flow was applied to the column can provide insight as to the liquid flow pattern in the column. This assumes that the liquid flow pattern remains relatively steady over the course of a scan, with the image stack being a time average. Several views of a flow model are shown in Figure 32. The liquid flow rate was  $36.7 \text{ m}^3/(\text{m}^2 \text{ h})$  ( $15.0 \text{ GPM}/\text{ft}^2$ ), and the vapor F-factor was  $1.59 \text{ Pa}^{0.5}$  [ $1.30 \text{ (ft/s)(lb}_m^{0.5}/\text{ft}^{1.5})$ ].

Several interesting features can be noted in the flow model images. When considering the angle view of the packing element, the corrugated sheets appear slightly wider and significantly brighter than for the dry case in Figure 30. This difference can be contributed to the presence of water on the surface. Also, there are some fuzzy regions along the surface of the packing and visible in the flow channels. These can represent small regions of liquid that existed for a portion of the scan. Faint circular regions of material can be seen when looking down the flow channel. These are the volumetric equivalent of image artifacts due to flow.

The apparent packing thickness and some artifacts are also visible in the top-down view. However, the most interesting aspects of that particular view are the appearance of the packing surface and the perforations. The surface texturing that was apparent in the dry images does not appear here in the flow reconstructions. Rather, a different pattern that resembles waves is visible. This likely indicates the presence of a water film on the surface of the packing sheets for the majority of the scan.

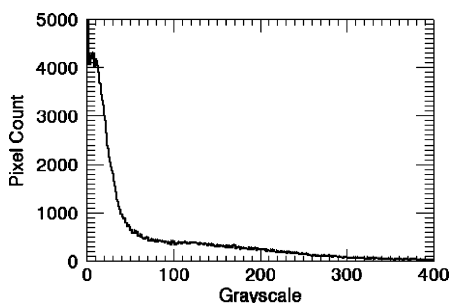


Figure 36. Histogram for CT image of liquid flow via subtraction, from which a threshold grayscale of 50 was chosen.

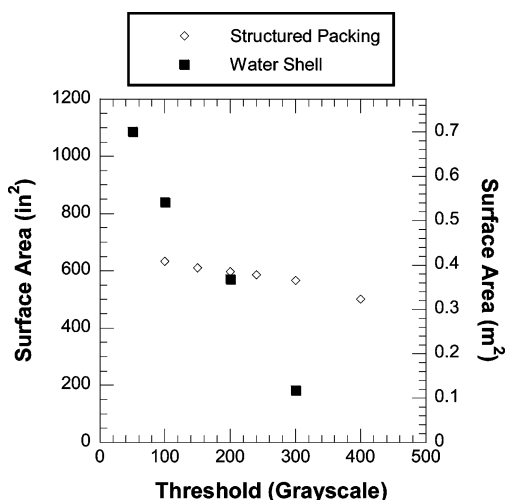


Figure 37. Dependence of surface area on threshold grayscale for structured packing and liquid shell.

When the column is observed under operation, regions of packing visible near the wall show the liquid films to continuously ripple. Additionally, the perforations on the sheets appear smaller and fuzzier than in the dry images. If liquid films were flowing over the perforations during the scan, the resulting images would exhibit behavior similar to what is observed. Clearly, the area around the perforations must be changing over the course of the scan for the resolution to differ this much from the dry case.

Considering again the joint area, an image similar to Figure 31 was created to evaluate the difference between the packing appearances near the joint for dry and flow cases. With the region above the interface exhibiting much higher holdup than the rest of the element, it would be expected that the 3-D model of the region would contain interesting features related to liquid accumulation. Unfortunately, it is difficult to discern areas of liquid accumulation in the region between corrugated sheets. The packing sheets themselves exhibit a surface pattern similar to that observed for the bulk element in Figure 33. Similarly, the sheets appear somewhat thicker and brighter, and the perforations appear smaller and less resolved than in the dry images. Circular artifacts can be seen in the left-hand side of the element. While excellent in reproducing images of dry packing, the image-stack technique does not capture the small-scale flow features necessary to visualize the liquid flow pattern itself or gross accumulations of liquid within an element.

Because each model consists of a large series of discrete CT slices, it is possible to apply the 2-D image analysis techniques for void fraction and liquid holdup discussed previously. Evaluating these parameters for a large data set permits a more detailed understanding of the flow behavior in the column as a

whole, rather than solely on a local level. Plotting the two values together as shown in Figure 34 allows elevations of interest in one data set to be directly compared to the other data set.

Figure 34 indicates that the void fraction profile in the packed bed follows an oscillatory pattern. The period of the regular oscillations is equal to the distance between perforations on the packing sheets. As expected, the void fraction is lower at elevations where no perforations are located and higher when the slice plane is located within a perforated region. It may also be noted that, from a height roughly from 40.6 to 45.7 cm (16.5–18 in.), the void fraction profile shifts somewhat lower. This region of the column contains a wiper band. The presence of extra material in this region will decrease the apparent void fraction.

In terms of liquid holdup, the packing joint areas can be clearly identified by the large spikes. Just above the interface, the holdup can be nearly 3 times the value observed in the packing bulk. The lowest holdup appears to be located just below the top of a packing element. The holdup is not constant through the middle portion of the element, however. The holdup profile and void fraction profile appear to be related. This is independent of the calculation method, since the holdup and void fraction were both normalized over the entire column cross section. In some areas where the void fraction exhibits a maximum, the holdup exhibits a minimum. In other regions, the holdup remains constant or increases when the void fraction increases. This could indicate that the liquid intermittently flows over the perforations.

**3.4. Surface Area from X-ray CT Isosurfaces.** In order to perform numerical analysis on the volumes created from individual CT slices, it was necessary to establish a continuous description of the surfaces contained in the images, rather than just a visual representation. The process of creating an isosurface from a volumetric data set requires the selection of a characteristic threshold value. The threshold defines the location of the surface to be created. The surface will be calculated and constructed in such a way that data with values below the threshold will be on one side of the plane and data with values higher than the threshold will be located on the opposite side of the plane.

To benchmark the surfacing procedure, a set of dry model data for the air–water contactor was considered. In order to ensure that the surface constructed represented the packing as desired, the 2-D CT data were cropped just inside the column wall. A total of 390 slices were used, representing 9.9 cm (3.9 in.) of the packed section height. The goal was to model and calculate the area available in one Mellapak 250Y half element. The stack was broken up into four sections to reduce the computational load.

A histogram was obtained for the data set to determine the distribution of grayscale values, including the maximum and minimum. For the dry case, cropping the images inside the column wall limits the materials being considered to air and packing. Since many of the data values were partial volume forms of packing, the threshold grayscale value needed to be chosen low enough to include the voxels fractionally filled by metal, yet exclude air pixels with values at the high end of the characteristic distribution. In an ideal two-phase system, the histogram peaks for each phase would be very sharp, narrow, and distinct, and the optimal threshold to differentiate between the two phases would be the grayscale located halfway between the peaks. However, the structured packing system presents a unique challenge because the packing sheets are so thin. This results in a broad distribution of grayscale values representing



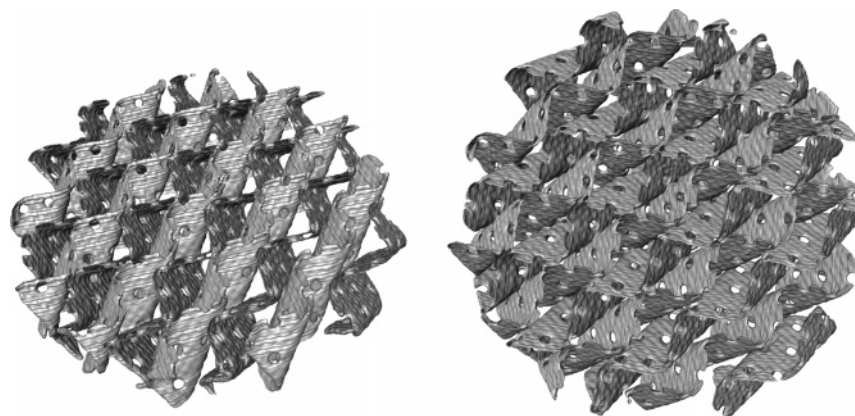


**Figure 38.** Views of an isosurfaced half element of Mellapak 250Y using a threshold grayscale of 150.

partial volume effects that overlaps with the distribution of air pixels. Thus, selection of the threshold is more complex. By analyzing the histogram in Figure 35, a threshold value of 150 was chosen to distinguish the structured packing surface. The peak near 40 represents air, with a much smaller and broader peak centered at 400 representing the structured packing. If the right-hand side of the air peak is extended to the  $x$ -axis, it appears to intersect at an approximate grayscale of 100. In order to ensure that no air pixels were included in the packing surface, the threshold was chosen slightly higher, near the region where the left side of the broad peak of packing pixels begins to taper off. The normal distribution of packing pixels extrapolates to intersect the  $x$ -axis near a grayscale of 200.

Once a threshold value was obtained, the surface could be created, viewed, and used for calculations. Amira contains a built-in module for the calculation of surface area and volume occupied by a surface. If too high a threshold were chosen, portions of the packing would be excluded from the isosurface. Conversely, if too low a threshold was used, then pixels representing air would be included when creating the surface, introducing error. The surface area calculated from the isosurfaced CT images was compared to the vendor-specified surface area.

A similar procedure was applied to CT subtraction images to evaluate the interfacial area between air and water in the packed bed. A series of difference images was created by subtracting the slices of a dry model from flow model slices where the liquid rate was  $36.7 \text{ m}^3/(\text{m}^2 \text{ h})$  ( $15.0 \text{ GPM}/\text{ft}^2$ ) and the vapor F-factor was  $1.59 \text{ Pa}^{0.5}$  [ $1.30 \text{ (ft/s)}(\text{lb}_m^{0.5}/\text{ft}^{1.5})$ ]. The subtraction data was cropped close to the inside of the column wall, and the resulting phases for analysis were limited to water and air. The interfacial area derived from the CT subtraction isosurface was compared to model predictions for packing fractional area and experimental data for reactive surface area obtained in a packed bed.

The choice of a threshold for water proved more difficult than choosing the threshold for packing. A significant portion of the water images represented partial volume and partial time conditions, which resulted in a large number of pixels with low grayscale values. The threshold determination required a decision to be made regarding how close to the characteristic values of air one could go before blurring the line between partial volume or time water pixels and noisy air pixels. Variations in average air and water grayscales over the course of the scan were also important considerations. Again, an image histogram was consulted to determine the proper threshold grayscale. The histogram for a sample subtraction image is shown in Figure 36.

The distribution of grayscales is quite different for the subtraction images than for the images of dry structured packing. The air peak has been shifted to the left, and a large number of pixels with a grayscale of zero are present. The subtraction process can act as a noise filter, resulting in pixels with negative grayscales. Such pixels are mapped to a grayscale of zero when the subtraction image is created, thus artificially increasing the population. Clearly the pixels representing water and air are overlapping, and no clear peak is evident for water. The characteristic grayscale value typically used for analysis of water pixels is  $\sim 180$ . To eliminate artificial noise being introduced to the water isosurface, the threshold was chosen to be 50. This value was located near the far right edge of the air peak when extrapolated to the  $x$ -axis and was low enough to include a good portion of the liquid phase. Choosing the threshold any higher would not capture all water pixels, but choosing any lower would introduce artificial surface from air and artifact pixels.

Figure 37 shows the dependence of surface area on threshold grayscales for both dry packing surface area and the surface area of the water shell extracted from CT images obtained under flow. The surface area of structured packing does not depend on the threshold value to the extent that the water shell surface area does. As a lower threshold value is specified, the surface becomes larger and computational time increases dramatically.

On the basis of observations of the image histograms and isosurface components at different thresholds, the values of 150 and 50 were chosen for packing and water, respectively. For water, it seems sensible to go to the lowest possible grayscale to include as many partial volume and partial time pixels as possible, with the limit approaching the characteristic grayscale of air in addition to flow artifacts. For packing, choosing a smaller grayscale will eventually only make the packing isosurface appear thicker and begin to include artifacts.

Determination of the expected surface area for the structured packing involved more than using the vendor-specified value. The surface area calculated from the isosurface would contain some area due to the wiper band. However, not all of the wiper-band area would contribute to the surface because of loss during the cropping procedure. Sulzer Chemtech, supplier of the packing, does not include the wiper-band area in the specified surface area. Also, area lost due to perforations is not accounted for in the vendor-supplied surface area value of  $250 \text{ m}^2/\text{m}^3$  ( $76.2 \text{ ft}^2/\text{ft}^3$ ). A correction was applied to account for lost area, with the value chosen as the true value of the packing sheet surface area being 85% of the vendor-specified value. The additional area provided by the wiper band was calculated based on the geometry of the band, which was added to the vendor-specified area twice to account for both sides of the band. The resulting

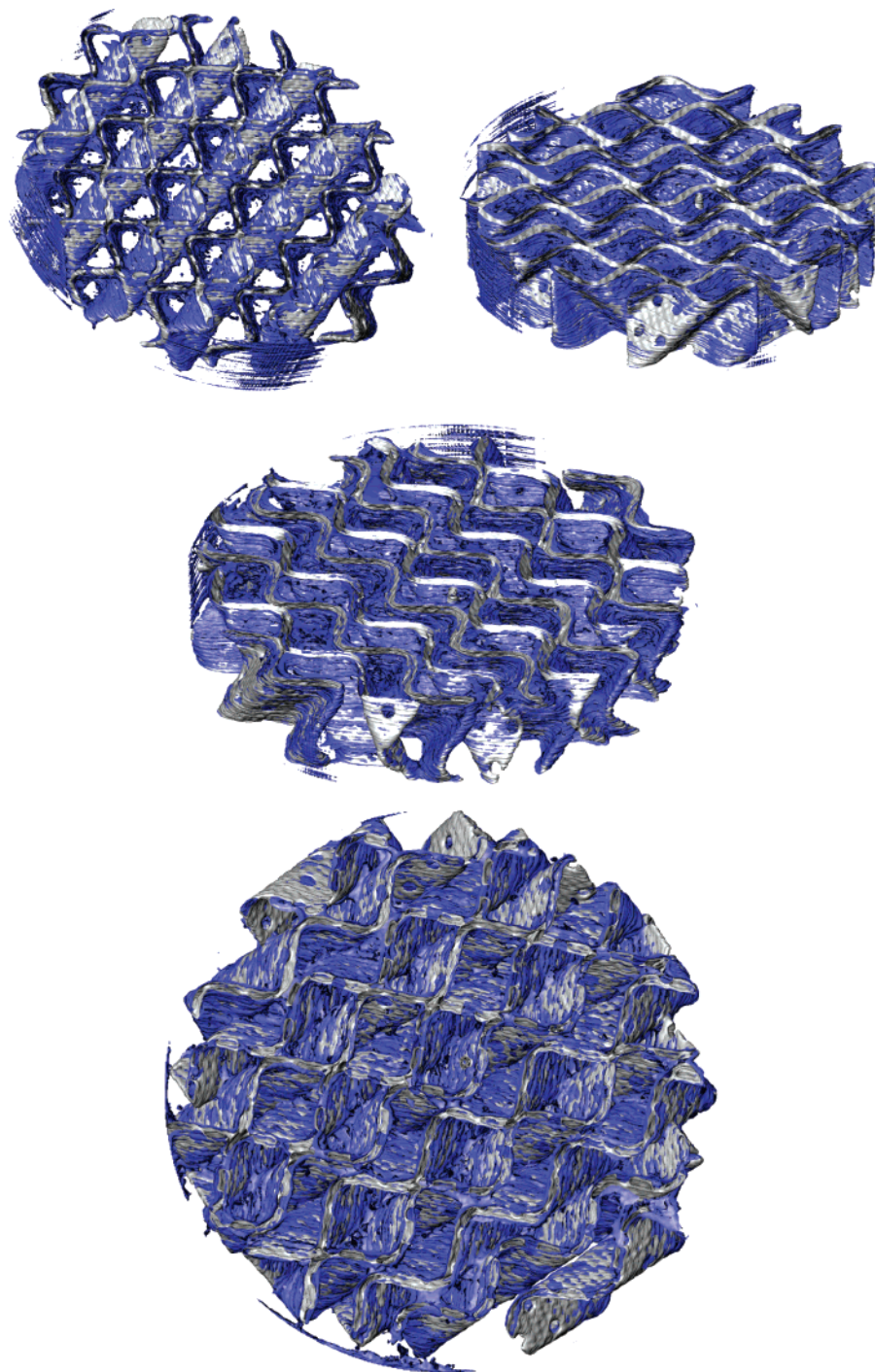


**Figure 39.** Liquid layer isosurface overlaid on dry packing image stack. Liquid rate is  $36.7 \text{ m}^3/(\text{m}^2 \text{ h})$  (15.0 GPM/ft<sup>2</sup>), and vapor F-factor is  $1.59 \text{ Pa}^{0.5}$  [ $1.3 \text{ (ft/s)(lb}_m^{0.5}/\text{ft}^{1.5})$ ].

expected area totaled to  $0.395 \text{ m}^2$  (612.5 in<sup>2</sup>) for the 9.9 cm (3.9 in.) tall section being considered, which equates to a specific surface area of  $238 \text{ m}^2/\text{m}^3$  (72.6 ft<sup>2</sup>/ft<sup>3</sup>). The area measured from the isosurface created using a threshold value of 150 was  $0.394 \text{ m}^2$  (610.5 in<sup>2</sup>), which is within 1% of the expected surface area. Obviously the agreement could change based on the choice of threshold, but the variation in area from thresholds from 100 to 240 was still within 5% of the expected value. Figure 38 shows the isosurface created with a threshold value of 150.

When the water isosurface was created using a threshold grayscale of 50, the resulting surface resembled the shape and structure of the packing element itself, indicating that the majority of the liquid flow through the bed is on the surface of the packing as a film. However, particularly near the bottom of

the shell, accumulations of liquid were surfaced inside the flow channels. It is this liquid that represents the portions of increased holdup near the packing element joint that could not be resolved using the standard image stack approach. The total surface area for the water shell was calculated to be  $0.702 \text{ m}^2$  (1088 in<sup>2</sup>).

In order to directly compare this value to experimental data for fractional area, it is necessary to apply certain assumptions. First, the surface area measured by isosurfacing the CT images that resulted from the subtraction of dry CT slices from flow CT slices is the entire surface area of the liquid shell. However, if film flow is assumed throughout the packed bed, then the interfacial area can be presumed equal to one-half of the total liquid surface area measured. The thickness of the film is

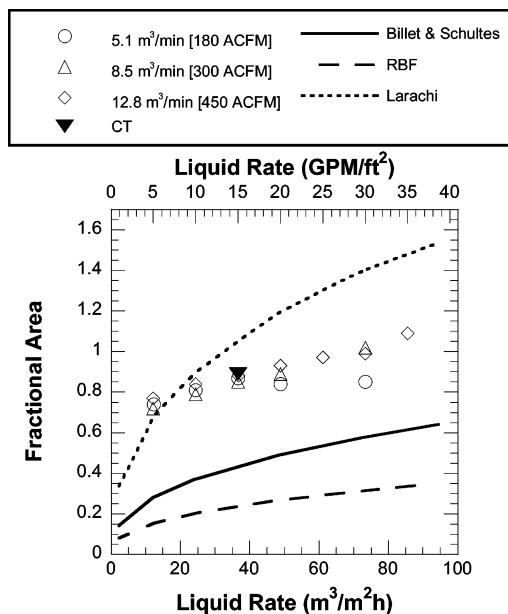


**Figure 40.** Comparison of experimental values and model predictions for fractional area in Mellapak 250Y. CO<sub>2</sub>/caustic absorption data taken from Seibert et al.<sup>11</sup>

assumed to be small, meaning that area on the edges of the film is negligible compared to the free surface area. Also, one side of the liquid film remains in contact with the metal packing surface and, therefore, does not exhibit an interface with the vapor phase. This accounts for the factor of one-half. The second caveat is that, when comparing the area obtained from isosurfacing to experimental data collected for the absorption of carbon dioxide into a dilute aqueous solution of sodium hydroxide, some deviation should exist. The absorption technique measures the reactive area, which, because of flow in the system, may not be the same as the interfacial area on the packing surface.

A composite image showing the liquid isosurface overlaid in blue on a 2.54 cm (1 in.) tall 3-D image stack reconstruction of dry packing is provided as Figure 39. The angled view down the flow channels confirms that some liquid accumulates between the packing sheets, either because of variation in flow pattern or from liquid holdup associated with the packing joint. The surface tension effects associated with water can be observed where the liquid meniscus is visible in the valley of several channels. The blue areas indicate regions where liquid existed for a long portion of the scan. Areas that do not show blue could have contained water, but likely for only a small portion of the scan time.

Packing near the middle of the column appears to be wetted to a greater extent than packing near the column wall. In the top-down view, the blue areas appear to exhibit a wavy texture similar to that seen in Figures 32 and 33, supporting the claim that the wavy texture is indicative of flow. Liquid branching near the contact points of the packing sheets is evident in the side views. The top-down view also lacks perforations in the center of the column, yet they appear near the perimeter of the packing. This suggests that perforations could be intermittently covered by liquid flow, as was previously suggested.

The measured area for the liquid shell was converted to fractional area by first dividing by two under the assumptions stated previously. The resulting value for interfacial area was divided by the packing surface area calculated from the isosurfaces of dry CT images. The isosurface data was plotted along with fractional area calculated from absorption experiment data and three predictive models for effective area. The

isosurfaces predicted a fractional area of 0.89, which was within 2% of the experimental values obtained using the CO<sub>2</sub> absorption method used by Seibert et al.<sup>11</sup> None of the models accurately fits the experimental data. The model of Billet and Schultes<sup>12</sup> and the Rocha-Bravo-Fair<sup>9,10</sup> correlation both severely underpredict fractional area, while the correlation of Iliuta, Petre, and Larachi<sup>13</sup> overpredicts fractional area, particularly at higher liquid rates. The results of the comparison are shown in Figure 40.

## 4. Conclusions and Future Work

**4.1. Conclusions.** The experimental results clearly demonstrate the ability of X-ray CT to obtain fundamental flow field data for an operating process unit. Without new methods of gathering process data from nontraditional sources for validation, the development of improved models can only go so far. The X-ray CT technique presented has shown promise in quantifying the interaction between vapor and liquid in a packed column in a nonintrusive manner. Purely hydraulic studies for model development can provide a link to understanding the underlying physics of multiphase flow. In addition, these experiments are not subject to any restrictions imposed by the need to first determine a mass transfer relationship.

Imaging experiments can do more than provide unique data. They can also be tailored to validate results gathered by traditional means, other novel approaches, and simulations. The liquid holdup profiles observed throughout the packed section indicate that local hydraulic behavior has a large impact on the stability of the column during the approach to flood. Manufacturers and modelers can leverage those phenomena to develop new theories about column operation. The development of high capacity structured packings that possess a modified transition zone between adjacent elements is one example. While it only provides a single data point, the agreement of the CT result for interfacial area with the results presented for the absorption of carbon dioxide into dilute caustic serves to validate the chemical technique. That experiment is much easier to run and can be used at almost any scale. The existing correlations for predicting fractional area will need to be improved to arrive at an ultimate rate-based model. X-ray CT is but one tool that can be utilized to proceed in that direction.

Together, the two methods have much potential to evaluate almost any type of column internal that can be fathomed. The insight gained from this project will assist packing designers as they attempt to maximize the contacting area while minimizing the packing capital cost. Fast volumetric characterization of actual packing elements can be realized with the latest generation of X-ray scanning equipment. The industry is on the verge of a step change in the rate of data acquisition and the amount of information available from a single experiment.

Ultimately, the quest for a "snapshot" of an operating contactor under any operating condition imaginable is feasible. Data of that type has never before been available. Such a capability is critical to necessary advances in model development, as distillation will continue to remain the workhorse of separation processes.

**4.2. Future Work.** The imaging experimental program continues to benefit from advances in X-ray technology. As the current program neared its conclusion, GE developed a new detector array based on flat panel geometry and a cone-beam X-ray source. This configuration allows 3-D X-ray scans to be obtained for a significant fraction of the packing volume in a single rotation. The resulting reduced scan times (typically on



the order of 1–2 min) will eliminate any uncertainty caused by flow field shifts during the scan acquisition period. A faster scan time also permits operation of the column at higher gas rates into the loading and flooding regime, although resolving stochastic rivulets and droplets will continue to prove difficult. In addition to the X-ray CT experimental program, a computational fluid dynamics based simulation of the gas-only flow through a structured packing element is being validated using an X-ray based particle tracking approach.

The application of X-ray imaging to a commercial fluid system is possible. Hydraulic studies using air and water have long been criticized for the inability to replicate the surface interaction seen in hydrocarbon systems. The high surface tension of water compared to hydrocarbons suggests that the flow patterns realized in this study may be quite different from those observed using a system more inclined to spread across the packing sheets. The relatively large corrugation length of the Mellapak 250Y used for this work limited capillary effects. The ability to modify the physical properties of the liquid phase would provide a new level of insight into column hydraulic behavior on a local level.

### Acknowledgment

The authors would like to thank the staff of the GE Aviation Manufacturing & Quality Technology Department located in Cincinnati, Ohio. Financial support from the US Department of Energy's Office of Energy Efficiency and Renewable Energy, Industrial Technologies Program, is gratefully acknowledged along with in-kind support from Dow Chemical, Sulzer Chemtech, Praxair, KochGlitsch, and Fluent.

### Literature Cited

(1) ASTM E1441-97: *Standard Guide for Computed Tomography (CT) Imaging*; American Society for Testing and Materials: West Conshohocken, PA, 1997.

- (2) Herman, G. T. *Image Reconstruction from Projections: The Fundamentals of Computerized Tomography*; Academic Press: New York, 1980.
- (3) Leahy, R. M.; Clackdoyle, R. Computed Tomography. In *Handbook of Image & Video Processing*; Bovik, A., Ed.; Academic Press: San Diego, CA, 2000; pp 771–787.
- (4) Rosenfeld, A.; Kak, A. C. *Digital Picture Processing*; Academic Press: San Diego, CA, 1982.
- (5) Jain, A. K. *Fundamentals of Digital Image Processing*; Prentice Hall, Inc.: Englewood Cliffs, NJ, 1989.
- (6) Cartmel, D. B. Investigation of Local Scale Phenomena in Vapor Liquid Contactors Using X-ray Tomography. M.S.E. Thesis, The University of Texas at Austin, Austin, TX, 1999.
- (7) Schmit, C. E. Evaluation of X-ray Imaging to Investigate Hydraulic Performance of Vapor–Liquid Contactors. Ph.D. Thesis, The University of Texas at Austin, Austin, TX, 2001.
- (8) Stichlmair, J.; Bravo, J. L.; Fair, J. R. General Model for Prediction of Pressure Drop and Capacity of Countercurrent Gas/Liquid Packed Columns. *Gas Sep. Purif.* **1989**, 3, 19–28.
- (9) Rocha, J. A.; Bravo, J. L.; Fair, J. R. Distillation, Columns, Containing, Structured, Packings: A Comprehensive Model for Their Performance. 1. Hydraulic Models. *Ind. Eng. Chem. Res.* **1993**, 32 (4), 641–651.
- (10) Rocha, J. A.; Bravo, J. L.; Fair, J. R. Distillation Columns Containing Structured Packings: A Comprehensive Model for Their Performance. 2. Mass-Transfer Model. *Ind. Eng. Chem. Res.* **1996**, 35 (5), 1660–1667.
- (11) Seibert, A. F.; Wilson, I.; Lewis, C.; Rochelle, G. Effective Gas/Liquid Contact Area of Packing for CO<sub>2</sub> Absorption/Stripping. Presented at the 7th International Conference on Greenhouse Gas Control Technologies, Vancouver, Canada, 2004; pp 1925–1928.
- (12) Billet, R.; Schultes, M. Prediction of Mass Transfer Columns With Dumped and Arranged Packings. *Chem. Eng. Res. Des.* **1999**, 77, 498–504.
- (13) Iliuta, I.; Petre, C. F.; Larachi, F. Hydrodynamic Continuum Model for Two-Phase Flow Structured-Packing Containing Columns. *Chem. Eng. Sci.* **2004**, 59 (4), 879–888.

Received for review January 31, 2007  
 Revised manuscript received May 29, 2007  
 Accepted June 5, 2007

IE0701827